

# Application of a Maximum-Entropy-Based 14-Moment Closure for Multi-Dimensional Non-Equilibrium Flows

Boone R. Tensuda\* and Clinton P. T. Groth †

*University of Toronto Institute for Aerospace Studies, Toronto, Ontario, M3H 5T6, Canada*

James G. McDonald‡

*University of Ottawa, Ottawa, Ontario, K1N 6N5, Canada*

The predictive capabilities of a new, 14-moment, maximum-entropy-based, interpolative closure are explored for multi-dimensional non-equilibrium flows with heat transfer. Unlike the maximum-entropy closure on which it is based, the interpolative closure provides closed-form expressions for the closing fluxes. While still presenting singular solutions in regions of realizable moment space, the interpolative closure proves to have a large region of hyperbolicity while remaining tractable. Furthermore, its singular nature is deemed advantageous for practical simulations. An implicit finite-volume procedure is proposed and described for the numerical solution of the 14-moment closure on two-dimensional computational domains, followed by a presentation and discussion of the results of a numerical dispersion analysis. Multi-dimensional applications of the closure are then examined for several canonical flow problems in order to provide an assessment of the capabilities of this novel closure for a range of non-equilibrium flows. The computational performance of the implicit solver is compared to a semi-implicit method. The predictive capabilities of the 14-moment interpolative closure were found to surpass those of the 10-moment Gaussian closure. It was also found to predict interesting non-equilibrium phenomena, such as counter-gradient heat flux. The implicit solver showed improved computational performance compared to the previously studied semi-implicit technique.

## Nomenclature

$a$	Speed of sound	$L$	Characteristic length
$A$	Area of cell	$m$	Particle mass
$\mathbf{A}$	Flux Jacobian	$M$	General macroscopic property (moment)
$\mathcal{A}$	Accommodation coefficient	$\mathbf{M}$	Vector of moments
$c_d$	Coefficient of Drag	$\mathcal{M}$	Maxwell-Boltzmann distribution function
$c_i$	Random velocity vector, $c_i = v_i - u_i$	$n$	Time step index
$c_p$	Heat capacity at constant pressure	$\hat{n}$	Unit vector normal
$c_v$	Heat capacity at constant volume	$n_w$	Number density at wall
$f$	Fill level	$p$	Hydrostatic pressure
$\mathcal{F}$	Phase-space distribution function	$\mathbf{P}$	Preconditioning matrix
$\mathcal{F}^{(14)}$	14-moment distribution function	$P_{ij}$	Anisotropic pressure tensor
$\mathbf{F}_k$	Flux dyad	Pr	Prandtl number
$g$	Temperature jump distance	$q_i$	Heat-flux vector
$\mathcal{G}$	Gaussian distribution function	$Q_{ijk}$	Generalized heat-flux tensor
$\mathbf{J}(\mathbf{U}^n)$	Residual Jacobian	$r$	Kurtosis
$k$	Cell face index	$R$	Specific gas constant
$K$	Thermal conductivity	$R_{ijkl}$	Fourth-order moments
Kn	Knudsen number, $\text{Kn} = \lambda/L$	$\mathbf{R}(\mathbf{U})$	Residual

\*M.A.Sc. Student, University of Toronto Institute for Aerospace Studies, 4925 Dufferein Street, Toronto, Ontario, Canada.

†Professor, University of Toronto Institute for Aerospace Studies, 4925 Dufferein Street, Toronto, Ontario, Canada, Senior Member AIAA.

‡Professor, Mechanical Engineering, University of Ottawa, 161 Louis Pasteur, Ottawa, Ontario, Canada.

$S$	Source term	$\mu$	Dynamic viscosity
$S_{ijklm}$	Fifth-order moments	$\xi$	Tuning coefficient
$t$	Time	$\rho$	Density
$U_w$	Wall velocity	$\sigma$	Parabolic surface mapping coefficient
$\mathbf{U}$	Conserved variables	$\tilde{\sigma}$	Lower $\sigma$ limit
$u_i$	Bulk velocity vector	$\tau$	Relaxation time
$\mathbf{v}$	Velocity magnitude, $v_i v_i$		
$v_i$	Particle velocity vector	<i>Subscript</i>	
$W$	Velocity weighting	*	Non-dimensionalized value
$\mathbf{W}$	Velocity weighting vector	Int	Interior flow field quantity
$x_i$	Position vector	$i, j$	Cell indices
$\alpha$	Maximum-entropy distribution coefficients	Kn	Knudsen layer quantity
$\gamma$	Ratio of specific heats, $c_p/c_v$	$L$	Lower plate quantity
$\Delta l$	Length of cell face	( $L$ )	Left state property
$\Delta t$	Time step	$m$	Quantity midway between plates
$\epsilon$	Convergence tolerance of Newton's method	( $R$ )	Right state property
$\zeta$	Convergence tolerance of GMRES	$U$	Upper plate quantity
$\Theta_{ij}$	Anisotropic temperature tensor, $\Theta_{ij} = P_{ij}/\rho$	$w$	Wall quantity
$\kappa$	Wavenumber	<i>Superscript</i>	
$\lambda$	Eigenvalue	( $L$ )	Left state property
$\Lambda$	Mean free path	$N$	Number of transport equations
$\lambda^-$	Minimum wave speed	( $R$ )	Right state property
$\lambda^+$	Maximum wave speed		

## I. Introduction and Motivation

The prediction of transition-regime non-equilibrium flows has proven to be a challenging branch of study in computational fluid dynamics (CFD). Transition-regime flows are encountered in a variety of engineering scenarios including: upper atmosphere flight or orbital reentry,<sup>1</sup> flows in micro-electromechanical systems (MEMS),<sup>2,3</sup> chemical vapour deposition in semi-conductor manufacturing, and the study of internal shock structure.<sup>4,5</sup> These high-Knudsen-number flows cannot be modelled using typical continuum approaches, such as the Euler and Navier-Stokes-Fourier (NSF) equations. Traditional methods for modelling non-equilibrium flows, such as direct simulation Monte Carlo (DSMC) methods<sup>6</sup> and techniques involving direct discretization of the Boltzmann equation,<sup>7</sup> are limited by their high computational cost, especially when applied in the transition regime. The DSMC technique models a large number of representative particles, and therefore will suffer from slow convergence when many particles are needed. The downfall of solving the discretized Boltzmann equation is its high dimensionality, which leads to high computational cost; especially for physically realistic three-dimensional cases.

The method of moment closures offers an alternative technique for accurately treating transition-regime flows with the potential of greater robustness and a significantly reduced computational cost. The moment closure method considers an assumed form of the particle distribution function to avoid modelling individual particles. It yields an approximation to the Boltzmann equation that consists of a finite set of partial differential equations (PDEs). These equations are of lower dimensionality as compared with the Boltzmann equation, and thus computational cost is reduced. Furthermore, the purely hyperbolic and first-order quasi-linear nature of some moment closures also presents several numerical advantages which extend into both the transition and continuum regimes.<sup>8</sup> These hyperbolic systems are less sensitive to grid irregularities, making them well suited to adaptive mesh refinement (AMR) and complex geometries. They also only require evaluating first derivatives, which means that an extra order of spatial accuracy, relative to a mixed hyperbolic-parabolic system, can be gained using the same stencil.

A hierarchy of moment closures having a number of desirable properties has been proposed by Levermore based on the maximization of thermodynamic entropy.<sup>9,10</sup> Unfortunately, complications encountered when considering higher-order moments, such as heat transfer, have severely limited the use of these maximum-entropy closures for general non-equilibrium flows. Recently, new, interpolative-type, maximum-entropy-based, 5-moment (one-dimensional gas) and 14-moment (three-dimensional gas) closures, initially investigated by McDonald and Groth,<sup>11</sup> and expanded upon by McDonald and Torrilhon,<sup>12</sup> have been proposed that successfully navigate the aforementioned problems. This study will present numerical results

from a further investigation of this new interpolative 14-moment closure technique via a mathematical dispersion analysis of the governing moment transport equations. The applicability of the 14-moment closure to multidimensional flows will also be examined by solving several two-dimensional canonical flow problems. As such, this study represents one of the first applications of the closure to multi-dimensional flows.

This paper will begin with a summary of relevant gas kinetic theory and the moment closure technique with attention to the maximum-entropy closure hierarchy (Section II). The 14-moment, maximum-entropy-based, interpolative-type closure is presented in Section III. The finite-volume procedure and implicit time marching scheme utilized to solve the 14-moment closure on two-dimensional computational domains is discussed in Section IV, and the associated boundary condition technique is presented in Section IV.D. The description and results of a dispersion analysis of the 14-moment system are discussed in Section V.A, and multi-dimensional cases of Couette flow, conduction between heated flat plates, subsonic flow past a circular cylinder, and lid-driven cavity flow are presented in Sections V.B, V.C, V.D, and V.E, respectively. Finally, in Section VI, conclusions are made based on the results of the dispersion analyses and multi-dimensional flow problems, and possible future work is suggested.

## II. Background

### II.A. Gas Kinetic Theory and Moment Closures

The following section presents the relevant background theory on gas kinetics and moment closures for monatomic gases. When discussing non-equilibrium gases it is convenient to make use of a non-dimensional parameter known as the Knudsen number,  $\text{Kn}$ . The Knudsen number is defined as the ratio between the mean free path of particles,  $\Lambda$ , and a characteristic length scale,  $L$ :  $\text{Kn} = \Lambda/L$ . Its value is inversely proportional to the frequency of collisions in the gas, and therefore also represents the gases distance from local equilibrium. Gases with small Knudsen numbers ( $\text{Kn} < 0.1$ ) experience many collisions, and thus will be near equilibrium, this is the so-called continuum regime. Conversely, gases with large Knudsen numbers ( $\text{Kn} > 100$ ) will have a negligible number of collisions; this is known as the free-molecular regime. The transition regime ( $0.1 < \text{Kn} < 100$ ) lies between, and presents the largest challenges in modelling. It is in this regime that moment closures show the most promise. In this regime non-equilibrium phenomena will be non-negligible, however the number of particles is still large enough that DSMC can be prohibitively expensive.

The method of moment closures relies on the field of gas kinetic theory, which was pioneered by Maxwell and Boltzmann.<sup>13,14</sup> This theory is built on the concept of a phase-space distribution function,  $\mathcal{F}(x_i, v_i, t)$ , which represents the probability of finding a single particle with a velocity,  $v_i$ , at a position,  $x_i$ , at time,  $t$ . The most well known of such phase-space distribution functions is the Maxwell-Boltzmann distribution,  $\mathcal{M}(v_i)$ , which describes the phase-space distribution of a monatomic gas in local thermodynamic equilibrium. All other possible phase-space distributions will tend to evolve toward the Maxwellian over time due to the effects of inter-particle collisions. The evolution of the distribution function is fully described by the Boltzmann equation<sup>14,15</sup>

$$\frac{\partial \mathcal{F}}{\partial t} + v_i \frac{\partial \mathcal{F}}{\partial x_i} = \frac{\delta \mathcal{F}}{\delta t}, \quad (1)$$

where  $\mathcal{F}(x_i, v_i, t)$  has been written as  $\mathcal{F}$  for brevity and it has been assumed that there are no external acceleration fields.

The term,  $\delta \mathcal{F}/\delta t$ , in Equation (1) is known as the collision term and represents the change of the distribution function as a result of inter-particle collisions. It is often formally expressed using the Boltzmann collision integral, which assumes molecular chaos, exclusively binary collisions, and a spherically symmetric force between particles that obeys classical mechanics.<sup>15-17</sup> However, even with such assumptions the Boltzmann collision integral is still very complex and expensive to evaluate. For this reason the simple Bhatnagar–Gross–Krook (BGK) approximation has been used in this study.<sup>18</sup> Using the BGK approximation the collision term becomes

$$\frac{\delta \mathcal{F}}{\delta t} \approx -\frac{\mathcal{F} - \mathcal{M}}{\tau}, \quad (2)$$

where  $\tau$  is a characteristic relaxation time scale. Although a very simple representation, the BGK approximation maintains the correct collisional invariants at equilibrium ( $\mathcal{F} = \mathcal{M}$ ), and is in agreement with

Boltzmann's H-theorem, meaning that entropy increases throughout the evolution. In this study the characteristic relaxation time is approximated as,  $\tau = \mu/p$ , where  $\mu$  is the dynamic viscosity of the gas, and  $p$  is the hydrostatic pressure. The fact that the BGK collision term uses only a single relaxation time implies that the Prandtl number of the gas considered,  $Pr$ , is always unity.

Macroscopic properties of a gas can be found by taking velocity moments of the phase-space distribution function,<sup>19</sup>

$$M(x_i, t) = \iiint_{-\infty}^{\infty} mW(v_i)\mathcal{F} dv_i = \langle mW(v_i)\mathcal{F} \rangle, \quad (3)$$

where  $M(x_i, t)$  is the value of the considered macroscopic property,  $m$  is the mass of a gas particle, and  $W(v_i)$  is the corresponding velocity weight. The macroscopic moments which will be referred to in this paper are:

$$\begin{aligned} \rho &= \langle m\mathcal{F} \rangle, & \rho u_i &= \langle mv_i\mathcal{F} \rangle, \\ P_{ij} &= \langle mc_i c_j \mathcal{F} \rangle, & Q_{ijk} &= \langle mc_i c_j c_k \mathcal{F} \rangle, \\ R_{ijkl} &= \langle mc_i c_j c_k c_l \mathcal{F} \rangle, & S_{ijklm} &= \langle mc_i c_j c_k c_l c_m \mathcal{F} \rangle, \end{aligned} \quad (4)$$

where  $\rho$  is the mass density,  $u_i$  is the bulk velocity,  $c_i = v_i - u_i$  is the random velocity,  $P_{ij}$  is the anisotropic pressure tensor,  $Q_{ijk}$  is the generalized heat-flux tensor, and  $R_{ijkl}$  and  $S_{ijklm}$  represent fourth- and fifth-order moments, respectively. Other convenient macroscopic properties can be related to contractions of these moments,

$$\begin{aligned} p &= \frac{1}{3} \langle mc_i c_i \mathcal{F} \rangle, \\ q_i &= \frac{1}{2} \langle mc_i c_j c_j \mathcal{F} \rangle, \\ r &= \frac{1}{15} \langle mc_i c_i c_j c_j \mathcal{F} \rangle, \end{aligned} \quad (5)$$

where  $p$  is the hydrostatic pressure,  $q_i$  is a general heat-flux vector, and  $r$ , the fully contracted fourth-moment, is related to the 'kurtosis' of the distribution function.

The transport equations for macroscopic properties are found by taking the appropriate moments of the Boltzmann equation. In general, a set of  $N$  transport equations can be found by defining a vector of  $N$  velocity weights,  $\mathbf{W}(v_i) = [W_0(v_i), W_1(v_i), W_2(v_i), \dots, W_N(v_i)]^T$ . The resulting transport equations, known as Maxwell's equations of change, are

$$\frac{\partial}{\partial t} \langle m\mathbf{W}\mathcal{F} \rangle + \frac{\partial}{\partial x_i} \langle v_i m\mathbf{W}\mathcal{F} \rangle = \langle m\mathbf{W} \frac{\delta\mathcal{F}}{\delta t} \rangle. \quad (6)$$

The first term,  $\partial\langle m\mathbf{W}\mathcal{F} \rangle/\partial t$ , is the time rate of change of the solution vector, the second term,  $\partial\langle v_i m\mathbf{W}\mathcal{F} \rangle/\partial x_i$ , is the divergence of the flux of the solution vector, the so-called flux dyad, and the final term,  $\langle m\mathbf{W}\delta\mathcal{F}/\delta t \rangle$ , is the source of the considered macroscopic property resulting from inter-particle collisions. It should be noted that the flux dyad always contains moments of one higher order than the solution vector, and thus the equation system is not closed. This implies that in order to solve the Boltzmann equation for an arbitrary phase-space distribution an infinite number of moments must be taken. This is not feasible and approximate methods, which yield a finite set of transport equations, must be used. This technique of approximating the Boltzmann equation using a finite set of transport equations is known as a moment closure.

In order to close the system of moment equations, the unknown closing flux(es) must be related to known moments. Typically this is done by assuming a form for the phase-space distribution which is a function of only known moments. This technique was pioneered by Grad,<sup>20</sup> who suggested a distribution of the following form

$$\mathcal{F} = \mathcal{M}[1 + \mathcal{P}^{(N)}(c_i)], \quad (7)$$

where  $1 + \mathcal{P}^{(N)}(c_i)$  is a Hermite expansion function about the equilibrium Maxwellian with respect to the random particle velocity.<sup>10</sup> This closure has been applied with success when considering near equilibrium distributions. However, it is possible for the assumed distribution function to become negative, which is nonphysical. Also, as the assumed distribution strays further from equilibrium, there is a loss of hyperbolicity

of the resulting moment equations, and a closure breakdown.<sup>8</sup> The Chapman-Enskog closure is an alternative technique which assumes that the distribution is in the form of a small perturbation about the equilibrium Maxwellian distribution.<sup>21,22</sup> Depending on the order of the perturbation this technique can be used to form the Euler, Navier-Stokes, Burnett, and Super-Burnett equation systems. Since these closures are based on only small perturbations from the Maxwellian, they break down for moderate and large departures from equilibrium.

## II.B. Maximum-Entropy Closures

The closures discussed thus far have all arrived at an assumed distribution function through an expansion about the equilibrium distribution. More recently, an alternative moment closure technique, known as the maximum-entropy closure, has been proposed.<sup>9,10</sup> This closure technique assumes a phase-space distribution function which maximizes thermodynamic entropy, and is therefore the most likely distribution, while remaining consistent with a given set of moments. The resulting form of the distribution is

$$\mathcal{F} = e^{\alpha^T \mathbf{W}}, \quad (8)$$

where  $\alpha$  is a set of coefficients that ensure agreement with the moment constraints. The values of the coefficients can be obtained by solving the constrained entropy-maximization problem,<sup>9</sup>

$$\frac{\partial}{\partial \alpha} [\langle e^{\alpha^T \mathbf{W}^{(N)}} \rangle - \alpha^T \mathbf{M}^{(N)}] = 0, \quad (9)$$

where  $\mathbf{M}$  is a vector of the macroscopic moments considered. This is a numerically expensive problem that must be solved at each flux evaluation.

When solving the maximum-entropy problem, it must be ensured that the phase-space distribution function remains realizable. To ensure moment realizability the given set of moments should, as a minimum, correspond to a set that could arise from a bounded and strictly positive distribution. Physical realizability can be maintained by ensuring that the matrix  $\mathbf{Y} = \langle m \boldsymbol{\Omega} \boldsymbol{\Omega}^T \mathcal{F} \rangle$  is positive definite.<sup>8,23,24</sup> The velocity weighting  $\boldsymbol{\Omega}$  in  $\mathbf{Y}$  is chosen such that all considered moments are contained in  $\mathbf{Y}$ , and is not necessarily equivalent to  $\mathbf{W}$ . Closures of this type offer the advantage of being hyperbolic whenever the maximum-entropy problem can be solved. Since they are not based on an expansion about the Maxwellian they can potentially be applied to gases far from equilibrium.

The two lowest-order members of the maximum-entropy hierarchy are the Maxwellian and Gaussian closures. For these two closures, the entropy maximization problem can be solved in closed form, thus the resynchronization procedure of Equation (9) need not be used. The Maxwellian closure generates the familiar Euler equation system, which is not applicable in non-equilibrium regimes. The Gaussian equation system extends from the Maxwellian by including a non-zero deviatoric stress term, thus viscous effects in non-equilibrium are accounted for.<sup>25</sup> Numerical solutions to the Gaussian closure using Godunov-type finite-volume methods have been studied by Brown *et al.*<sup>26</sup> and McDonald and Groth,<sup>8,27</sup> and generate reliable results in both the continuum and transition regimes when heat transfer is not important. Heat transfer has been introduced in the Gaussian closure using a Chapman-Enskog like expansion by McDonald and Groth,<sup>28</sup> however this regularization technique results in the addition of elliptic terms to the moment equations. In order to add heat transfer while maintaining hyperbolicity, super-quadratic velocity weightings must be used in the maximum-entropy distribution's velocity weighting vector,  $\mathbf{W}$ .

Unfortunately, problems with the maximum-entropy closure arise when higher-order, super-quadratic, velocity terms, which describe heat transfer, are added. Firstly, the maximum-entropy problem ceases to have a closed-form analytic solution and relatively expensive iterative approaches are required to relate macroscopic moments and closure coefficients. Furthermore, and more limiting, regions in physically realizable moment space develop within which the maximum-entropy problem cannot be solved as the approximate distribution does not remain bounded.<sup>29</sup> The highest-order closing fluxes become singular as this space is approached. This unrealizable subspace will be referred to as the Junk subspace. These complications have limited the use of the maximum-entropy closure technique for general non-equilibrium flows. However, a new interpolative-type closure,<sup>12,23</sup> has shown success in navigating these problems and is the primary focus of the present numerical study.

### III. The 14-Moment Interpolative Closure

As mentioned above, recently an interpolative-type closure based on the maximum-entropy hierarchy has been proposed.<sup>12,23</sup> The velocity weighting vector used for this closure is  $\mathbf{W} = [1, v_i, v_i v_j, v_i \mathbf{v}^2, \mathbf{v}^4]$ , where  $\mathbf{v} = v_i v_i$ . For a monatomic gas, this leads to a set of 14-moment equations, which include a non-zero heat-flux vector, in the form

$$\frac{\partial \mathbf{U}}{\partial t} + \frac{\partial \mathbf{F}_k}{\partial x_k} = \mathbf{S}, \quad (10)$$

where  $\mathbf{U}$  is the vector of conserved variables,  $\mathbf{F}_k$  is the flux dyad, and  $\mathbf{S}$  is the source vector resulting from inter-particle collisions modelled using the BGK operator. For a three-dimensional gas, these vectors are

$$\mathbf{U} = \begin{pmatrix} \rho \\ \rho u_i \\ \rho u_i u_j + P_{ij} \\ \rho u_i u_j u_k + u_i P_{jj} + 2u_j P_{ij} + Q_{ijj} \\ \rho u_i u_i u_j u_j + 2u_i u_i P_{jj} + 4u_i u_j P_{ij} + 4u_i Q_{ijj} + R_{iiij} \end{pmatrix}, \quad (11)$$

$$\mathbf{F}_k = \begin{pmatrix} \rho u_k \\ \rho u_i u_k + P_{ik} \\ \rho u_i u_j u_k + u_i P_{jk} + u_j P_{ik} + u_k P_{ij} + Q_{ijk} \\ \rho u_i u_k u_j u_j + u_i u_k P_{jj} + 2u_i u_j P_{jk} + 2u_j u_k P_{ij} + u_j u_j P_{ik} + u_i Q_{kjj} + u_k Q_{ijj} + 2u_j Q_{ijk} + R_{ikjj} \\ \rho u_k u_i u_i u_j u_j + 2u_k u_i u_i P_{jj} + 4u_i u_i u_j P_{jk} + 4u_i u_j u_k P_{ij} + 2u_i u_i Q_{kjj} + 4u_i u_k Q_{ijj} + 4u_i u_j Q_{ijk} \\ + 4u_i R_{ikjj} + u_k R_{iiij} + S_{kiiij} \end{pmatrix}, \quad (12)$$

$$\mathbf{S} = \begin{pmatrix} 0 \\ 0 \\ \frac{\delta_{ij} P_{kk} - 3P_{ij}}{3\tau} \\ \frac{2u_i (\delta_{ij} P_{kk} - 3P_{ij}) - 6u_i P_{jk} - 3Q_{ijj}}{3\tau} \\ \frac{1}{3\tau} \left( -3R_{iiij} + \frac{5P_{ii} P_{jj}}{\rho} - 12u_i Q_{ijj} + 4u_i u_j (\delta_{ij} P_{kk} - 3P_{ij}) \right) \end{pmatrix}. \quad (13)$$

It should be noted that the 14-moment system as presented above is not closed; to close the system the moments  $Q_{ijk}$ ,  $R_{ijkk}$ , and  $S_{ijjkk}$  in the flux vector must be approximated. In order to circumvent the problems associated with higher-order maximum-entropy closures, the interpolative closure of McDonald and Torrilhon<sup>12</sup> approximates these closing fluxes using closed-form expressions, as opposed to numerically solving the maximum-entropy problem. These closed-form expressions are found in three steps. Firstly, the region of realizability between the physical realizability boundary and Junk subspace is determined, and a suitable remapping of moments is employed. Information about the behaviour of the closing flux is then found at equilibrium and on the realizability boundaries. Finally, a closing flux is postulated which is consistent with the constraints at the boundaries and also transitions between them with values that approximate those found by solving the maximum-entropy problem numerically. The reader should refer to the paper by McDonald and Torrilhon<sup>12</sup> for additional information on the derivation of the 14-moment system and the closing fluxes.

It is convenient when forming the closing fluxes to define a parabolic surface mapping using an additional variable,  $\sigma$ , where  $\sigma$  is constant on paraboloids in realizable moment space, with  $\sigma = 1$  corresponding to the physically realizable boundary, and  $\sigma = 0$  corresponding to the Junk subspace. In this case,  $\sigma$  is related to the known moments such that the following equality is satisfied,

$$R_{iiij} = \frac{1}{\sigma} Q_{kii} (P^{-1})_{kl} Q_{ljj} + \frac{2(1-\sigma)P_{ji}P_{ij} + P_{ii}P_{jj}}{\rho} \quad \sigma \in [0, 1]. \quad (14)$$

Expressions for the closing fluxes as a function of known moments can then be postulated using the interpolative method summarized above and fully described by McDonald and Torrilhon.<sup>12</sup> The resulting closing fluxes are

$$Q_{ijk} = \frac{\partial Q_{ijk}}{\partial Q_{mnn}} Q_{mnn}, \quad (15)$$

where

$$\frac{\partial Q_{ijk}}{\partial Q_{mnn}} = [P_{il}(P^2)_{jk} + P_{kl}(P^2)_{ij} + P_{jl}(P^2)_{ik}] [P_{lm}(P^2)_{\alpha\alpha} + 2(P^3)_{lm}]^{-1}, \quad (16)$$

$$R_{ijkk} = \frac{1}{\sigma} Q_{ijl}(P^{-1})_{lm} Q_{mkk} + \frac{2(1-\sigma)P_{ik}P_{kj} + P_{ij}P_{kk}}{\rho}, \quad (17)$$

$$S_{ijjkk} = \frac{Q_{npp}Q_{mjj}Q_{ikl}}{\sigma^2 P_{kn}P_{lm}} + 2\sigma^{\frac{1}{2}} \frac{P_{jj}Q_{ikk}}{\rho} + (1-\sigma^{\frac{1}{2}})W_{im}Q_{mnn}, \quad (18)$$

with

$$W_{im} = \frac{1}{\rho} [P_{il}(P_{\alpha\alpha})^3 + 6P_{il}(P^3)_{\alpha\alpha} + 7(P^2)_{\alpha\alpha}(P^2)_{il} + 10P_{\alpha\alpha}(P^3)_{il} + 10(P^4)_{il} - (P^2)_{\alpha\alpha}P_{\beta\beta}O_{il} - 3(P_{\alpha\alpha})^2(P^2)_{il}] [P_{lm}(P^2)_{\alpha\alpha} + 2(P^3)_{lm}]^{-1}. \quad (19)$$

By inspection of Equation (18), it is clear that a singularity in the closing flux continues to be encountered at the Junk subspace (when  $\sigma = 0$ ), as was also the case in the original maximum-entropy closures. However, past research has found that this singular nature is advantageous in practical implementation.<sup>12</sup> It produces very large propagation speeds and was found to yield accurate solutions of stationary, one-dimensional, shock structure having smooth transitions, without undesirable sub-shocks, even for high Mach numbers.<sup>12</sup> The effect of the singularity on wave propagation speed is further explored in Section V.A. The singularity also motivates the use of a fully implicit solver, which is described in Section IV.C.

## IV. Numerical Solution of the 14-Moment Closure

This section describes details of both a semi-implicit and fully-implicit Newton–Krylov–Schwarz (NKS) solver for the 14-moment closure. The semi-implicit scheme has been used extensively in previous studies of the Gaussian, regularized Gaussian, and 14-moment closures.<sup>12, 28, 30, 31</sup> A NKS solver for the Gaussian and regularized Gaussian closures has also been developed in recent studies by Lam and Groth, and was found to significantly reduce computational cost.<sup>32</sup> A similar NKS solution procedure is applied here to the solution of the 14-moment closure. This represents the first study of the solution of this novel closure using NKS. The computational performance of the two methods will be compared in Section V.

### IV.A. Upwind Finite-Volume Scheme

The moment transport equation system of the 14-moment closure for two-dimensional planar flows on multi-block quadrilateral meshes can be solved using a parallel higher-order Godunov-type finite-volume scheme. After discretizing the spatial domain using the finite-volume method the system of moment transport equations can be written in a semi-discrete form, resulting in a coupled set of non-linear ordinary differential equations. At steady-state these equations are

$$\frac{d\mathbf{U}_{(i,j)}}{dt} = -\frac{1}{A_{(i,j)}} \left( \sum_k (\mathbf{F} \cdot \hat{n} \Delta l)_{(i,j,k)} \right) + \mathbf{S}_{(i,j)} = -\mathbf{R}(\mathbf{U}_{(i,j)}) = 0, \quad (20)$$

where  $\mathbf{U}_{(i,j)}^n$  and  $\mathbf{S}_{(i,j)}^n$  are the solution vector of conserved variables and source vector, respectively, in cell  $(i, j)$ ,  $\mathbf{F}_k$  is the flux dyad,  $\Delta l$  is the length of the cell face,  $\hat{n}$  is the unit vector normal to the cell face,  $A_{(i,j)}$  is the area of cell  $(i, j)$ , and  $\mathbf{R}(\mathbf{U}_{(i,j)})$  is the residual.

The term,  $(\mathbf{F} \cdot \hat{n} \Delta l)_{(i,j,k)}$ , is the numerical flux at the  $k$ th cell face, which is found by approximately solving Riemann problems at the corresponding cell interfaces. The left and right solution states at the cell

interfaces required to solve the Riemann problem are found by extrapolating the cell-averaged quantities using a least-squares piece-wise limited linear solution reconstruction technique, with the Venkatakrishnan type limiter.<sup>33</sup> The HLL-type approximate Riemann solver<sup>34</sup> is then used to find an approximate solution to the Riemann problem, and thus a numerical flux. Using the HLL technique the intermediate flux at the cell interface,  $\mathbf{F}^{\text{HLL}}$ , is found as

$$\mathbf{F}^{\text{HLL}} = \frac{\lambda^+ \mathbf{F}_{\mathbf{L}} - \lambda^- \mathbf{F}_{\mathbf{R}}}{\lambda^+ - \lambda^-} + \frac{\lambda^+ \lambda^-}{\lambda^+ - \lambda^-} (\mathbf{U}_{\mathbf{R}} - \mathbf{U}_{\mathbf{L}}), \quad (21)$$

where  $\mathbf{F}_{\mathbf{R}}$  and  $\mathbf{F}_{\mathbf{L}}$  are the right and left fluxes,  $\mathbf{U}_{\mathbf{R}}$  and  $\mathbf{U}_{\mathbf{L}}$  are the right and left solution states, and  $\lambda^+$  and  $\lambda^-$  are the maximum and minimum solution wave propagation speeds, respectively. Typically, the maximum and minimum wave speeds are found using the eigenvalues of the flux Jacobian. However, due to the complexity of the 14-moment system, at this stage in development the maximum and minimum wave speeds are approximated based on the acoustic wave speeds in a monatomic gas. The approximate wave speeds at a cell interface with a normal in the  $x$ -direction are taken to be

$$\lambda^- = \min \left( u_x^{(\text{R})} - \xi \sqrt{\frac{\gamma P_{\text{xx}}^{(\text{R})}}{\rho^{(\text{R})}}}, u_x^{(\text{L})} - \xi \sqrt{\frac{\gamma P_{\text{xx}}^{(\text{L})}}{\rho^{(\text{L})}}} \right), \quad (22)$$

$$\lambda^+ = \max \left( u_x^{(\text{R})} + \xi \sqrt{\frac{\gamma P_{\text{xx}}^{(\text{R})}}{\rho^{(\text{R})}}}, u_x^{(\text{L})} + \xi \sqrt{\frac{\gamma P_{\text{xx}}^{(\text{L})}}{\rho^{(\text{L})}}} \right), \quad (23)$$

where the superscripts (R) and (L) denote properties at the right and left states, respectively,  $\gamma$  is the ratio of specific heats and equal to 5/3 for a monatomic gas, and  $\xi$  is a tuning coefficient which is set large enough that the scheme is stable, while remaining small enough to ensure there is not excess numerical dissipation or excessively small time steps. Due to the singular nature of the closing flux and numerical limitations, the values of  $\sigma$  must be limited, a lower limit of  $\tilde{\sigma} = 2.0 \times 10^{-4}$  is found to be sufficient. If  $\sigma$  becomes less than this value, it is then replaced with  $\sigma = \tilde{\sigma}$ . Both a semi-implicit and fully-implicit time marching method have been used to solve Equation (20), and the performance of each is compared in Section V.A.

#### IV.B. Semi-Implicit Scheme

As the continuum regime is approached the values of the relaxation time,  $\tau$ , can become very small, leading to excessive numerical stiffness of the system. This is alleviated by utilizing point-implicit time-marching.<sup>27</sup> This time-marching technique is applied to the semi-discrete ODE system (Equation 20). The resulting fully-discrete solution scheme is

$$\tilde{\mathbf{U}}_{(i,j)}^{n+1} = \mathbf{U}_{(i,j)}^n - \frac{\Delta t}{A_{(i,j)}} \left( \sum_k (\mathbf{F} \cdot \hat{n} \Delta l)_{(i,j,k)}^n \right) + \Delta t \tilde{\mathbf{S}}_{(i,j)}^{n+1}, \quad (24)$$

$$\mathbf{U}_{(i,j)}^{n+1} = \mathbf{U}_{(i,j)}^n - \frac{\Delta t}{2A_{(i,j)}} \left( \sum_k (\mathbf{F} \cdot \hat{n} \Delta l)_{(i,j,k)}^n + \sum_k (\tilde{\mathbf{F}} \cdot \hat{n} \Delta l)_{(i,j,k)}^{n+1} \right) + \Delta t \left( \frac{\mathbf{S}_{(i,j)}^n + \mathbf{S}_{(i,j)}^{n+1}}{2} \right), \quad (25)$$

where  $n$  is the temporal index and  $\Delta t$  is the time step.

#### IV.C. Newton–Krylov–Schwarz Algorithm

Due to the limit on the time step by the Courant–Friedrichs–Lewy condition,<sup>35</sup> explicit and semi-implicit methods, such as the algorithm described in Section IV.B, tend to have slow convergence for numerically stiff systems. Implicit methods however are unconditionally stable, and thus a much higher time step can be used, leading to a lower number of iterations needed to reach a steady-state solution. The trade-off is that each iteration now requires solving a linear system, which has large computational cost and memory requirements. However, various techniques have been developed to minimize the cost of solving this system, and for many problems the gain in time step size is sufficient to offset the added computational cost and memory requirement at each iteration.<sup>35</sup> Due to the stiffness of the proposed 14-moment system, especially

near the continuum regime (see Figure 3 in Section V.A), it is expected that an implicit solver will lead to improved computational performance.

An implicit scheme which has proven to be effective in solving a variety of transport equation systems is the Newton–Krylov–Schwarz (NKS) algorithm.<sup>36,37</sup> This algorithm is based on the well established Newton’s method, however the resulting linear system of equations is solved inexactly using the Krylov subspace iterative method GMRES (Generalized Minimal RESidual),<sup>38</sup> with a Schwarz type preconditioner.<sup>39</sup>

The nonlinear algebraic system of Equation (20) can be solved iteratively using Newton’s method. Based on an initial estimate at step  $n = 0$ , an improved solution at the next step,  $n + 1$ , is found as  $\mathbf{U}^{n+1} = \mathbf{U}^n + \Delta\mathbf{U}^n$ , where  $\Delta\mathbf{U}^n$  is the solution update. This update value is found by solving the linear system,

$$\mathbf{J}(\mathbf{U}^n)\Delta\mathbf{U}^n = -\mathbf{R}(\mathbf{U}^n), \quad (26)$$

where  $\mathbf{J}(\mathbf{U}^n)$  is the residual Jacobian. This procedure is iterated to generate improved steady state solutions until the solution residual is sufficiently small, i.e.,

$$\|\mathbf{R}(\mathbf{U}^{n+1})\|_2 < \epsilon \|\mathbf{R}(\mathbf{U}^0)\|_2, \quad (27)$$

where  $\epsilon$  is the convergence tolerance, typically  $10^{-6} - 10^{-11}$ .

The matrices considered are large, and thus direct solution of the linear system presented in Equation (26) is not feasible. For this reason approximate iterative methods are typically used. In particular the GMRES technique<sup>38</sup> has proven to be a robust and fast method for the solution of the large, sparse, and non-symmetric matrix associated with the linear system of Equation (26).<sup>40,41</sup> This equation can be rewritten in the more general form,  $\mathbf{Ax} = \mathbf{b}$ , where  $\mathbf{A} = \mathbf{J}(\mathbf{U}^n)$ ,  $\mathbf{x} = \Delta\mathbf{U}$ , and  $\mathbf{b} = -\mathbf{R}(\mathbf{U}^n)$ . The GMRES technique is an iterative projection method where solution updates are chosen from an orthogonalized Krylov subspace such that the L2-norm of the residual,  $\mathbf{r} = \mathbf{b} - \mathbf{Ax}$ , is minimized. This results in a two-tiered scheme containing an “inner” iterative GMRES linear solver and an “outer” iterative Newton’s method non-linear solver. In order to speedup the solver the requirements on the convergence of the GMRES solver are relaxed, such that the “inner” iterations are carried out only until

$$\|\mathbf{R} + \mathbf{J}\Delta\mathbf{U}\|_2 \leq \zeta \|\mathbf{R}\|_2, \quad (28)$$

where the convergence tolerance,  $\zeta$ , is set to a modest value between 0.01 and 0.5. This results in what is known as an inexact Newton’s method. Previous studies of such methods have found that it is not necessary to perform the linear solve exactly to still obtain rapid convergence of the Newton solver.<sup>42</sup>

The effectiveness of the GMRES algorithm for solving the system,  $\mathbf{Ax} = \mathbf{b}$ , can be increased by preconditioning. The preconditioned system is

$$(\mathbf{AP}^{-1})(\mathbf{Px}) = \mathbf{b}, \quad (29)$$

where  $\mathbf{P}$  is the preconditioning matrix. A good preconditioning matrix will approximate  $\mathbf{A}^{-1}$ , while being less expensive to invert than  $\mathbf{A}$ . In this study the additive Schwarz preconditioner<sup>38,43,44</sup> has been used. This is a domain-decomposition method, whereby the domain is separated into smaller blocks, and the solutions on these blocks are passed amongst each other and used as Dirichlet boundary conditions. Furthermore, a local block preconditioner is applied to each of these subdomains. This preconditioner is formed via incomplete lower-upper factorization on an approximate Jacobian of the solution residual for the considered block. In order to maintain a fast solver, the accuracy of the LU factorization is limited by a level of fill,  $f$ , of 2 or 3. This method of preconditioning couples well with the block-based parallelization and adaptive mesh refinement of the solver.<sup>45,46</sup>

The implementation of the NKS solver is based on that of Groth and Northrup.<sup>37,47</sup> This solver has already been successful for a number of equation systems, such as non-equilibrium flows evaluated with the Gaussian closure.<sup>32</sup> When applying this solver to the 14-moment interpolative closure the Jacobians which are required to obtain the local preconditioner have been approximated using finite differences, as opposed to exact algebraic expressions which are traditionally used. This is because of the complexity of the closing fluxes for this particular closure. This approximation is expected to have some detriment on the performance of the NKS scheme, however it is a good first step.

Although the results presented in this study are all found using the finite difference approximations for the Jacobians, there has been some investigation into analytically determined Jacobians herein. As a proof-of-concept, an analytic source-term Jacobian and flux-Jacobian were found which are valid in the continuum

regime. When formulating the flux-Jacobian it was assumed that the closing fluxes,  $R_{ijkk}$  and  $S_{ijjkk}$ , are constant. Since these are high-order moments it was expected that they will not have a significant influence in the continuum regime, and thus would seem justified. In numerical tests, the use of the analytic Jacobians was found to reduce CPU time requirements by a factor of 2-3 compared to the finite difference based Jacobians. This is promising and a more general procedure for the evaluation of Jacobians will be explored in further work.

#### IV.D. Boundary Conditions

Appropriate solid-wall boundary conditions for moment closure methods, which produce the correct non-equilibrium phenomena, are not obvious. Determining the boundary conditions at a solid wall is simplified by assuming that a Knudsen layer of infinitesimal thickness forms adjacent to the wall.<sup>20</sup> In this Knudsen layer, the particle distribution function is a combination of the distribution function of particles from the interior flow field and particles reflected from the solid wall. It is also assumed that particle reflection is either specular or diffusive. The probability of a diffusive interaction occurring is defined using an accommodation coefficient,  $\mathcal{A}$ . When  $\mathcal{A} = 0$  the interactions are exclusively specular, and particles will experience an elastic collision with the wall. When  $\mathcal{A} = 1$  the interactions will be exclusively diffusive, and particles will be fully accommodated by the wall before being reintroduced into the Knudsen layer with velocities described by a Maxwellian distribution, which depends on the wall's temperature and velocity.

Using these assumptions, a distribution function for the particles at the solid-wall boundary can be defined as

$$\mathcal{F}_{\text{Kn}} = \mathcal{F}_+ + \mathcal{F}_-, \quad (30)$$

where  $\mathcal{F}_{\text{Kn}}$  is the distribution of particles in the Knudsen layer,  $\mathcal{F}_-$  is the distribution of the particles entering the Knudsen layer from the interior flow field, and  $\mathcal{F}_+$  is the distribution of the reflected particles. Assuming that the wall lies parallel to the  $y$ -axis (see Figure 1), these distribution functions are

$$\mathcal{F}_- = \begin{cases} \mathcal{F}_{\text{int}}(v_x, v_y, v_z) & \text{if } v_x > 0, \\ 0 & \text{if } v_x < 0 \end{cases} \quad (31)$$

$$\mathcal{F}_+ = \begin{cases} \mathcal{A}\mathcal{M}_{\text{W}}(v_x, v_y, v_z) + (1 - \mathcal{A})\mathcal{F}_{\text{int}}(-v_x, v_y, v_z) & \text{if } v_x < 0, \\ 0 & \text{if } v_x > 0 \end{cases} \quad (32)$$

where  $\mathcal{F}_{\text{int}}$  is the distribution function of particles in the interior flow, and  $\mathcal{M}_{\text{W}}$  is the Maxwellian distribution of the particles accommodated by the wall,

$$\mathcal{M}_{\text{w}} = n_w \left( \frac{m}{2\pi k T_w} \right)^{\frac{3}{2}} e^{-\frac{m}{2k T_w} (v_x^2 + (v_y - u_{wy})^2 + v_z^2)}, \quad (33)$$

where  $T_w$  is the temperature of the wall,  $u_{wy}$  is the wall velocity, and  $n_w$  is the number density of the reflected Maxwellian. These distributions are used in conjunction with known properties at the wall, such as zero normal net flux, to find expressions for the moments in the Knudsen layer, which are then used to determine boundary conditions.

Since the 14-moment closure is formulated by postulating relations between the closing fluxes and known moments directly, as opposed to assuming a certain distribution function, it is not obvious what interior flow distribution,  $\mathcal{F}_{\text{int}}$ , should be used. However, since the closure is based on the maximum-entropy closure, it would be expected that the interior distribution would be near to a maximum-entropy distribution. In this study a Grad-like perturbative expansion applied to the Gaussian distribution function, a 10-moment maximum-entropy closure, has been used as the interior distribution.<sup>48-50</sup> This distribution has 14 free parameters and permits the direct evaluation of moments of all orders by analytical means. Thus, it is a natural choice to use with the present 14-moment interpolative closure.

The 14-moment Gaussian-based perturbative distribution is expressed as,

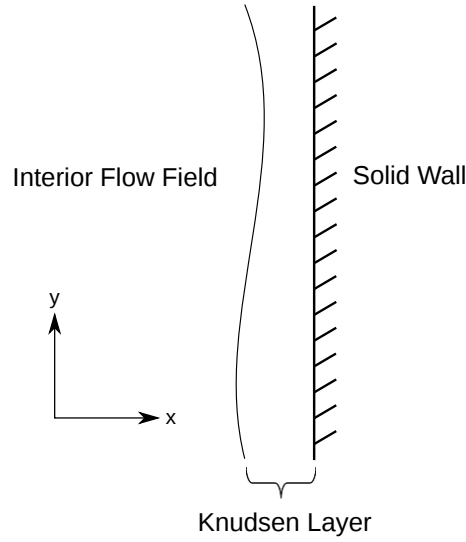


Figure 1: Representation of the Knudsen layer.

$$\mathcal{F}^{(14)} = \mathcal{G} \left[ 1 + \frac{D_\beta}{5} \left[ \Theta_{\alpha\beta}^{-1} \left( c_\alpha c^2 - \frac{P_{\gamma\gamma} c_\alpha}{\rho} \right) - 2c_\beta \right] + 3E \left( c^4 - 2\frac{P_{\alpha\alpha}}{\rho} c^2 - 4\frac{P_{\alpha\beta}}{\rho} c_\alpha c_\beta + \frac{P_{\alpha\alpha} P_{\beta\beta}}{\rho^2} + 2\frac{P_{\alpha\beta}^2}{\rho^2} \right) \right]. \quad (34)$$

where,  $\mathcal{G}$ , is the Gaussian distribution function, which by defining an anisotropic ‘temperature’ tensor,  $\Theta_{ij} = P_{ij}/\rho$ , can be expressed as

$$\mathcal{G} = \frac{\rho}{m(2\pi)^{3/2}(\det\Theta_{ij})^{1/2}} \exp\left(-\frac{1}{2}\Theta_{ij}^{-1}c_i c_j\right). \quad (35)$$

The coefficients,  $D_\alpha$  and  $E$ , are required to satisfy the following relations,

$$q_i = \frac{1}{5\rho} [P_{j\alpha}^2 D_i + 2P_{i\alpha} P_{j\alpha} D_j], \quad (36)$$

$$E = \frac{5\rho^3}{8} \frac{\mathcal{K}}{[P_{\alpha\gamma}^2 P_{\beta\delta}^2 + 2P_{\alpha\gamma} P_{\alpha\delta} P_{\beta\gamma} P_{\beta\delta}]}, \quad (37)$$

where,

$$\mathcal{K} = r - (P_{\alpha\alpha} P_{\beta\beta} + 2P_{\alpha\beta}^2) / 15\rho. \quad (38)$$

The 14-moment Gaussian-based perturbative distribution of Equation (34) is now used as the interior distribution,  $F_{\text{int}}$ , in Equations (31) and (32) to obtain values for the moments in the Knudsen layer. The resulting expressions are:

$$n_{\text{Kn}} = \frac{(2 - \mathcal{A})}{2\sqrt{\pi} P_{xx}^{3/2} m} \left\{ \sqrt{\pi} \rho P_{xx}^{3/2} - \frac{\sqrt{2}}{5} D_x \sqrt{\rho} (P_{xy}^2 + P_{xx}^2) \right\} + \frac{\mathcal{A} n_w}{2}, \quad (39)$$

$$u_{x\text{Kn}} = 0, \quad (40)$$

$$u_{y\text{Kn}} = \frac{-3(2-\mathcal{A})n}{2\sqrt{\pi}P_{xx}^{5/2}\rho^3n_{\text{Kn}}}\left\{\frac{\sqrt{2}}{15}\rho^{5/2}P_{xx}(D_xP_{xx}^2u_y - 5P_{xx}P_{xy} + D_xP_{xy}^2u_y) - \frac{\sqrt{\pi}}{3}\rho^3P_{xx}^{5/2}u_y\right. \\ \left. + \sqrt{2}E\sqrt{\rho}P_{xy}(P_{xx}^2 + P_{xy}^2)(P_{xx}^2 + 4P_{xx}P_{yy} - 3P_{xy}^2)\right\} + \frac{\mathcal{A}n_w}{2n_{\text{Kn}}}u_{wy}, \quad (41)$$

$$P_{xy\text{Kn}} = \frac{(2-\mathcal{A})}{2\sqrt{\pi}\rho^2P_{xx}^{3/2}}\left\{\frac{\sqrt{2}}{5}\rho^{3/2}[D_yP_{xx}^3 + D_xP_{xx}^2P_{xy} + P_{xx}P_{xy}(D_yP_{xy} + 2D_xP_{yy}) - D_xP_{xy}^3]\right. \\ \left. - \sqrt{2}\rho^{5/2}P_{xx}^2(u_{y\text{Kn}} - u_y) + \sqrt{\pi}\rho^2P_{xx}^{3/2}P_{xy} + 3\sqrt{2}E\sqrt{\rho}(P_{xx}^2 + P_{xy}^2)^2(u_{y\text{Kn}} - u_y)\right\} \\ - \mathcal{A}\sqrt{\frac{n_w\rho_wkT_w}{2\pi}}(u_{wy} - u_{y\text{Kn}}), \quad (42)$$

$$Q_{xii\text{Kn}} = \frac{9(2-\mathcal{A})\rho}{2\sqrt{\pi}\rho^4P_{xx}^{5/2}}\left\{\frac{2\sqrt{2}}{45}\rho^{5/2}P_{xx}\left[-P_{xx}P_{xy}\left(P_{xy}(D_yu_{y\text{Kn}} - D_yu_y - \frac{5}{2}) + 2D_xP_{yy}(u_{y\text{Kn}} - u_y)\right)\right.\right. \\ \left. + P_{xx}^3\left(5 + D_y(u_y - u_{y\text{Kn}})\right) + P_{xx}^2\left(-D_xP_{xy}(u_{y\text{Kn}} - u_y) + \frac{5}{2}P_{zz} + \frac{5}{2}P_{yy}\right) + P_{xy}^3D_x(u_{y\text{Kn}} - u_y)\right] \\ - \frac{\sqrt{2}}{3}E\rho^{3/2}P_{xx}(P_{xy}^2 + P_{xx}^2)^2(u_{y\text{Kn}} - u_y)^2 + \frac{4\sqrt{\pi}}{45}D_y\rho^2P_{xx}^{7/2}P_{xy} + \frac{\sqrt{2}}{9}\rho^{7/2}P_{xx}^3(u_{y\text{Kn}} - u_y)^2 \\ + \frac{8\sqrt{\pi}}{45}\rho^2P_{xx}^{5/2}\left(D_xP_{xy}^2 + P_{xy}\left(-\frac{5}{4}\rho u_{y\text{Kn}} + \frac{5}{4}\rho u_y + \frac{1}{2}D_yP_{yy}\right) + \frac{1}{4}D_x(P_{zz}^2 + P_{yy}^2)\right) \\ + \frac{2\sqrt{\pi}}{15}D_x\rho^2P_{xx}^{9/2} + \sqrt{2}\sqrt{\rho}\left(2P_{xx}^6 + \frac{1}{3}P_{xx}^4(19P_{xy}^2 + 4P_{zz}^2 + 4P_{yy}^2) + 2P_{xx}^3P_{xy}^2\left(P_{yy} - \frac{1}{3}P_{zz}\right)\right. \\ \left. - \frac{1}{3}P_{xx}^5(P_{zz} + P_{yy}) + \frac{8}{3}P_{xx}^2P_{xy}^2\left(\frac{1}{2}P_{zz}^2 + \frac{3}{2}P_{yy}^2 + P_{xy}^2\right) - 3P_{xx}P_{xy}^4(P_{yy} + \frac{1}{9}P_{zz}) + P_{xy}^6\right)E\left\} \\ - \frac{\mathcal{A}\rho_w\sqrt{kT_w}}{\sqrt{2\pi}m^{3/2}}\{m(u_{y\text{Kn}} - u_{yw})^2 + 4kT_w\}. \quad (43)$$

An interesting result of the formulated boundary conditions is the coupling between the shear stress,  $P_{xy}$ , and heat flux,  $Q_{xii}$  and  $Q_{yii}$ . The influence of the heat flux and shear stress in the interior fluid on the shear stress and heat flux in the Knudsen layer is explored in Figure 2. Figure 2 (a) depicts how the  $x$ -direction heat flux in the Knudsen layer changes as the shear stress of the interior fluid increases. In the equilibrium regime this shear stress is expected to be zero, however as the Knudsen number is increased the stress will also increase (this effect is seen in Figure 5 (b) of Section V.B). It is clear that in the equilibrium and near-equilibrium regimes, when the shear stress is small, the resulting heat flux in the Knudsen layer is also small. However, as the Knudsen number, and thus shear stress, is increased the heat flux in the Knudsen layer also increases rapidly. Additionally, as the heat flux parallel to the boundary increases, the shear stress in the Knudsen layer also increases as seen in Figure 2 (b). However, in this case the relationship is linear. In conclusion, it is found that at high Knudsen numbers the boundary conditions become tightly coupled.

## V. Numerical Results

### V.A. Dispersion Analysis and Maximum Wave Speeds

The solutions of hyperbolic relaxation systems of PDEs are in the form of waves. Therefore, when studying systems of such equations, understanding the properties of these waves is of great importance. Two such properties are the wave speed and damping rate. The PDE systems considered in moment closures exhibit dispersive wave behaviours, meaning that their wave speeds and damping are a function of the wavenumber of the propagating solution wave. In order to gain insight into what these wave speeds and damping rates are,

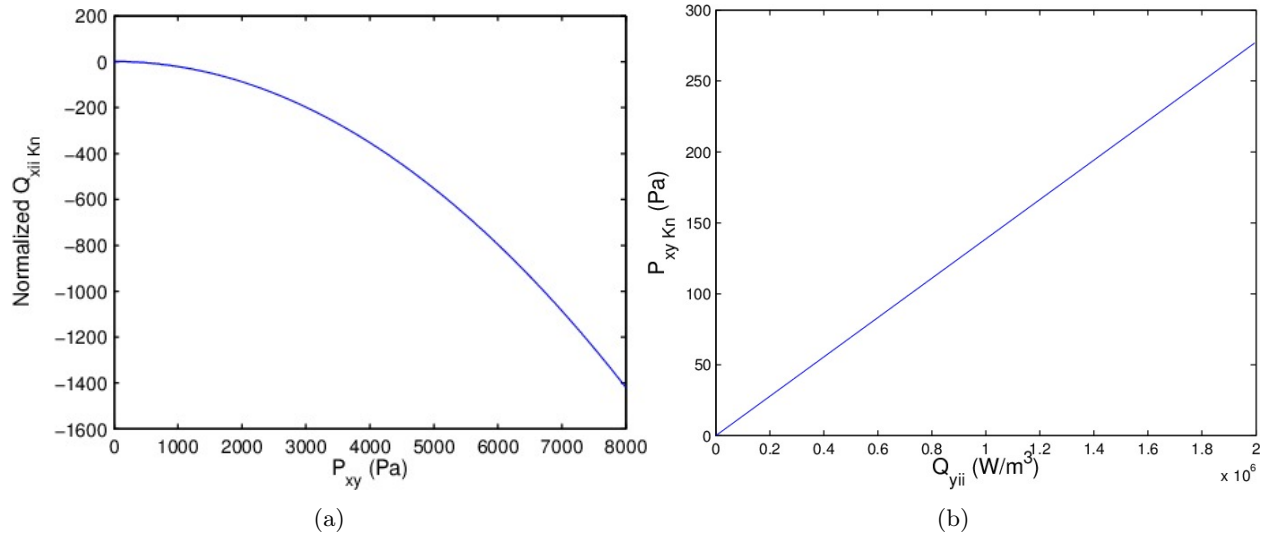


Figure 2: (a) Heat flux in the Knudsen layer, normalized with respect to the equilibrium value, as a function of the shear pressure in the interior fluid. (b) Shear pressure in the Knudsen layer as a function of heat flux parallel to the boundary. The remaining interior fluid properties are set to typical values for argon gas.

and how they vary with wavenumber, a dispersion analysis is performed. In general, a dispersion analysis describes how a certain linear operator acts on Fourier modes of perturbations with different wave numbers.<sup>51</sup> In the case of a system of PDEs in weakly conservative form this linear operator is  $\partial/\partial t + \mathbf{A}\partial/\partial x - \mathbf{Q}$ , where  $\mathbf{A}$  is the flux-Jacobian, and  $\mathbf{Q}$  is the source-term Jacobian. The perturbative solutions are assumed to be of the form

$$\mathbf{u}(x, t) = \text{Re} \left[ \mathbf{v}(t)e^{-ikx} \right], \quad (44)$$

where,  $\mathbf{v}(t)$  is the amplitude of the solution wave,  $k$  is the wavenumber, and  $i$  is  $\sqrt{-1}$ . The linearized differential operator applied to Equation (44) yields a set of ordinary differential equations (ODEs) given by

$$\frac{d\mathbf{v}}{dt} = (ik\mathbf{A} + \mathbf{Q})\mathbf{v}, \quad (45)$$

which has the non-trivial solution

$$\mathbf{v}(t) = e^{it(k\mathbf{A} + \mathbf{Q})} \mathbf{u}_0, \quad (46)$$

where  $\mathbf{u}_0$  is the initial amplitude of the solution. The wave speed and decay constants of this solution are proportional to the real and imaginary components of the eigenvalues of  $(k\mathbf{A} - i\mathbf{Q})$ , respectively. The wavenumber  $k$  can be related to the Knudsen number by  $\text{Kn} = 2\pi k$ ,<sup>26</sup> and therefore the properties of the solution waves can be determined for the entire range of Knudsen numbers.

A dispersion analysis, which is outlined above, was applied to the 14-moment interpolative closure for a monatomic gas with only variations in the  $x$ -direction and an axi-symmetric distribution function about the  $v_x$  axis, leading to moment relations:  $u_y = u_z = 0$ ,  $P_{xy} = P_{xz} = P_{yz} = 0$ , and  $Q_{yij} = Q_{zii} = 0$ . The particle distribution function is transformed such that  $u_x = 0$ , and the moments are non-dimensionalized such that  $\rho = P_{xx} = P_{yy} = P_{zz} = 1$ , these non-dimensionalized moments are denoted with a ‘ $\star$ ’ subscript.

Of particular interest are the maximum frozen wave speeds, which are the maximum wave speeds as  $\kappa \rightarrow \infty$ , since these values will limit the Mach numbers for which internal shock structures can be resolved without generating unphysical sub-shocks. They will also influence the stiffness of the system. For the Grad-13 and Gaussian closure the maximum frozen wave speeds at equilibrium have been found to be Mach 1.65 and Mach  $3/\sqrt{5}$ , respectively.<sup>10,26</sup> The 14-moment closure however has been found to provide smooth shock structure even up to Mach numbers of 8.<sup>12</sup> It is expected that the singularity in the closing flux encountered at the Junk subspace results in arbitrarily large frozen wave speeds as the subspace is approached, leading to smooth shock structures. This is confirmed by the dispersion analysis of the 14-moment system as shown

in Figure 3, which display the maximum frozen wave speeds on constant  $\sigma$  contours. Recall that  $\sigma$  is equal to zero at the Junk subspace, therefore the maximum wave speed is expected to increase as  $\sigma$  approaches zero. This behaviour is seen in Figure 3, although it is observed that the wave speeds reduce rapidly at points below equilibrium. These large wave speeds, especially near equilibrium, suggest that a fully implicit solution scheme may be ideal, due to the resulting stiffness of the equation system. The dispersion analysis is also performed at a single point very close to equilibrium ( $Q_{xix} = 0$  and  $R_{iijx} = 14.99$ ), since the presence of the Junk subspace prevents analysis exactly at equilibrium. The attenuation rate results are shown in Figure 4 (a). It is clear that these attenuation values remain between zero and one for all wavenumbers and thus the system is stable at all Knudsen numbers. The wave speed results are shown in Figure 4 (b). The wave speeds approach the speed of sound in the continuum regime, i.e., as  $\kappa \rightarrow 0$ , which is expected.

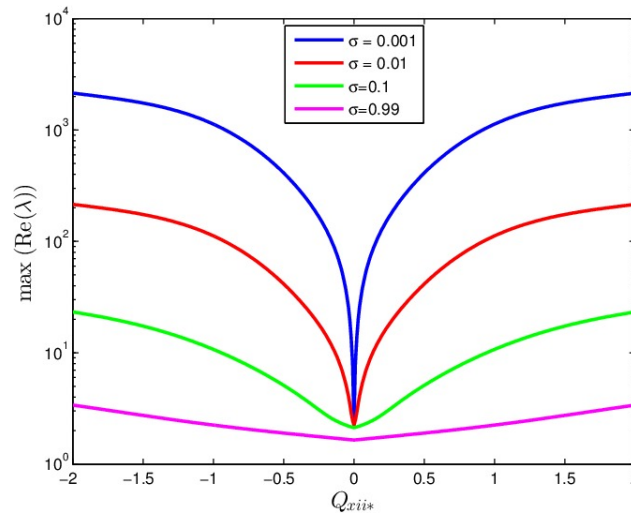


Figure 3: Maximum wave speed on constant  $\sigma$  contours for a gas with spatial variations in one direction.

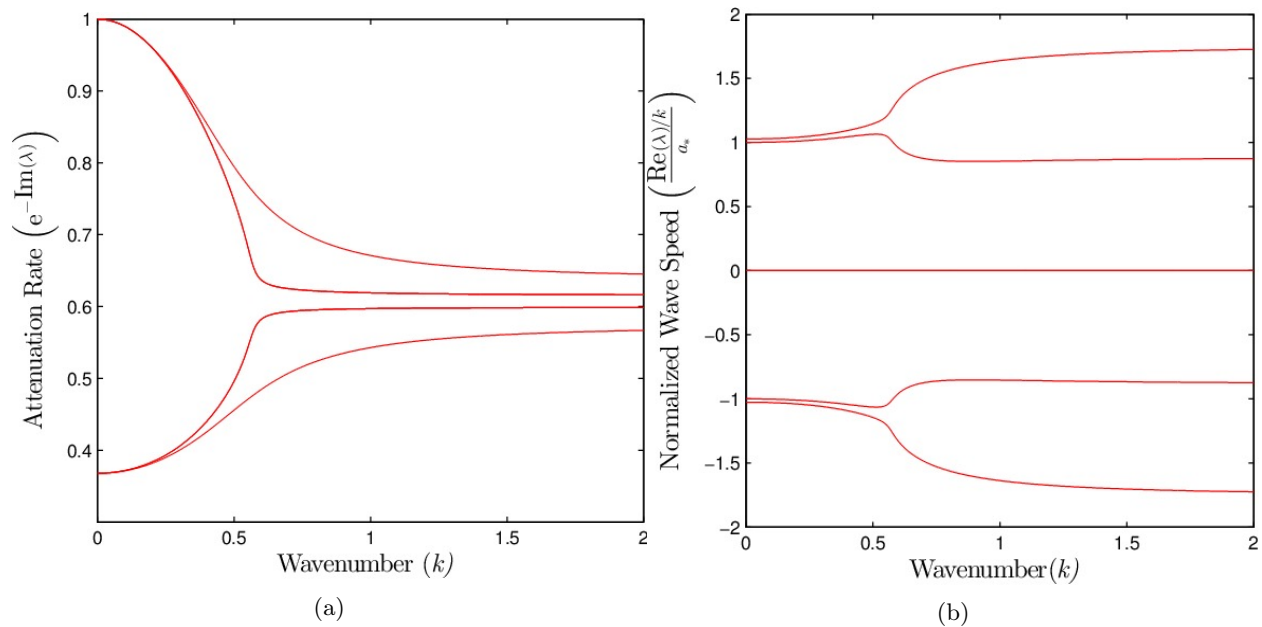


Figure 4: (a) Attenuation rate and (b) wave speed diagrams near equilibrium.

## V.B. Couette Flow

A good first test case for non-equilibrium models is that of planar subsonic Couette flow between two oppositely moving plates, as studied previously by McDonald and Groth<sup>8,27</sup> and McDonald *et al.*<sup>11</sup> The Knudsen number for this case is found as  $\text{Kn} = \Lambda/d$  where  $d$  is the distance between the plates, and the mean free path is given by

$$\Lambda = \frac{16\mu}{5\sqrt{2\pi\rho p}}. \quad (47)$$

This model of the mean free path assumes that the gas molecules interact as hard spheres.<sup>6</sup> For this case, the Knudsen number can be adjusted by simply changing the distance between the plates. It is expected that as the Knudsen number is raised, and the free-molecular regime is approached, the appearance of slip flow at the plates will become more pronounced, since fewer interactions between the gas and plate particles are occurring. The ability to recreate this slip flow accurately is a good benchmark for both the moment closure method and the boundary conditions considered.

The Couette flow case which has been considered consists of two parallel plates moving in opposite directions at a velocity,  $U_w$ , of 30 m/s in the  $x$ -direction. The gas between the plates is argon with standard atmospheric free stream density of 1.225 kg/m<sup>3</sup> and pressure of 101.325 kPa, and therefore a temperature of 397.37 K. The temperature of the plates,  $T_w$ , is 397.37 K to ensure minimal heat transfer between the plates and internal gas. The transport equations of the 14-moment closure, summarized in Section III, were solved using both the semi-implicit and NKS numeric algorithms described in Section IV, on a mesh containing 10 cells in the  $x$ -direction, and 100 cells in the  $y$ -direction, for a total of 1000 computational cells. Periodic boundaries were specified in the  $x$ -direction and the solid-wall half-Maxwellian boundary conditions, Equations (40)-(43), were specified at the plate surfaces. An accommodation coefficient of  $\mathcal{A} = 1$  was used. The results for the normalized flow velocity  $u_x/U_w$ , and normalized shear stress,

$$P_{xy}^* = \frac{-P_{xy}}{\rho U \sqrt{\frac{2kT}{\pi m}}}, \quad (48)$$

for a wide range of Knudsen numbers are shown in Figure 5. These computed values are compared with results found using the Gaussian closure,<sup>8</sup> and the analytical solution developed by Lees.<sup>52</sup> It is evident that the predicted values of the 14-moment closure are in very good agreement with those of the Gaussian and Lees solution throughout the continuum, transition, and free-molecular regimes. The figures also illustrate the failure of both the NSF equations and free-molecular solution in the transition regime, emphasizing the importance of moment closures and their ability to model gases throughout this regime.

A comparison between convergence histories for the semi-implicit and NKS solvers is presented in Figure 6. The L2-norm values are with respect to the density and are normalized by the residual value of the first iteration. The semi-implicit solver uses a CFL number of 0.5. The NKS solver shows improved performance over the semi-implicit scheme, with a factor of CPU time savings of between 3 and 11 times, for each of the Knudsen numbers considered. As discussed in Section V.A, the wave speeds become higher as the continuum regime is approached, i.e the Knudsen number is lowered, and based on this finding it was hypothesized that the performance of the NKS solver would be most pronounced in the continuum regime. Furthermore, in the continuum regime the relaxation time scales become very small, leading to additional stiffness of the system. As a result the  $\text{Kn}=0.01$  case shows an improved NKS performance relative to the semi-implicit scheme when compared to the  $\text{Kn}=0.1$  and  $\text{Kn}=1$  cases.

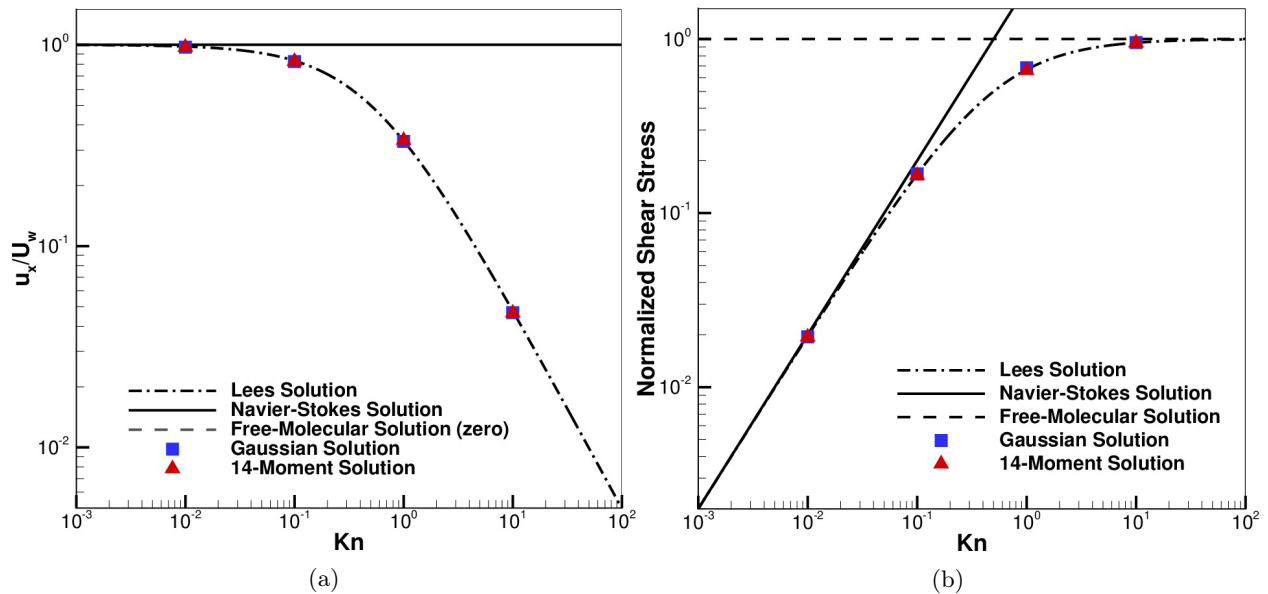


Figure 5: (a) Normalized flow velocity at the plate as a function of Knudsen number. (b) Normalized shear stress between the plates as a function of Knudsen number.

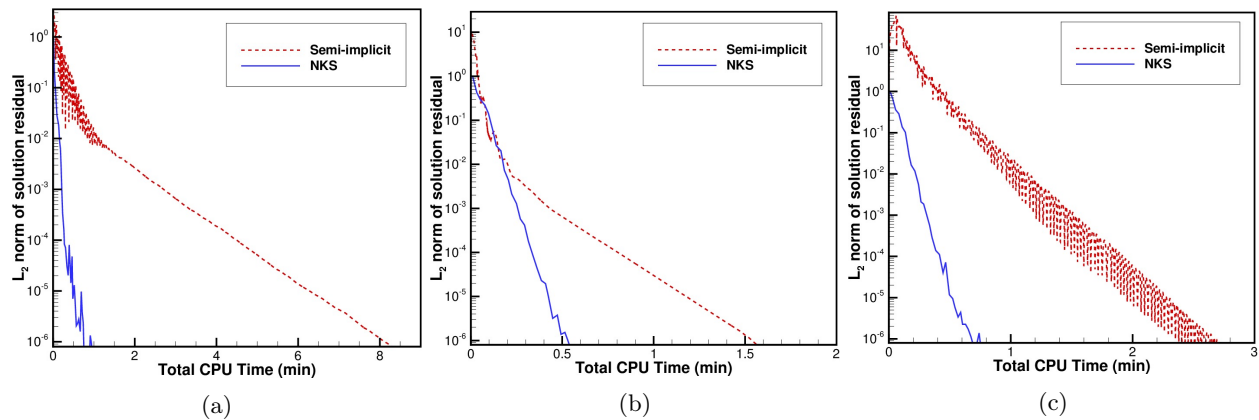


Figure 6: Comparison of convergence of the solution residuals for the NKS and semi-implicit solvers when applied to a Couette flow case with a Knudsen number of (a) 0.01, (b) 0.1, and (c) 1.

## V.C. Heat Conduction Between Infinite Plates

The case of heat conduction between two infinite flat plates oriented parallel to the  $x$ -axis has also been considered. In this case it is expected that in the continuum regime the temperature of the interior fluid adjacent to the wall will be equivalent to the wall temperature. However, as the Knudsen number is increased a temperature jump between the wall and internal fluid will develop, due to the reduced number of interactions between the internal gas particles and particles reflected from the plate. Accurately predicting this phenomena is a good benchmark for the 14-moment closure and heat-flux boundary conditions.

The gas between the heated plates is argon at a temperature of 397.37 K, density of 1.225 kg/m<sup>3</sup> and pressure of 101.325 kPa. The upper plate temperature,  $T_U$ , has been set to 407.37 K, and the lower plate temperature,  $T_L$ , has been set to 387.37 K; resulting in a temperature differential of 20 K between the plates. The computational domain consisted of 4 cells in the  $x$ -direction and 100 cells in the  $y$ -direction, for a total of 400 computational cells. The solid-wall half-Maxwellian boundary conditions, with  $\mathcal{A} = 1$ , were specified at the plate surfaces, and periodic boundaries were used in the  $x$ -direction. The values of normalized wall temperature,  $T^*$ , and normalized heat-flux between the plates were found for a large range of Knudsen numbers.

The numerical results for heat transfer between the two plates are presented in Figure 7. In the figure, the wall temperature has been normalized as

$$T^* = \frac{T - T_m}{T_w - T_m}, \quad (49)$$

where  $T$  is the temperature of the gas at the wall,  $T_m$  is the gas temperature midway between the plates, and  $T_w$  is the temperature of the plate. The temperatures at and adjacent to the lower plate are used to find  $T^*$ . Ideally it should not matter whether the upper or lower plate is used, however it was found that at large Knudsen numbers there was a small discrepancy. The suspected mechanism leading to this discrepancy will be further discussed below. The heat flux between the plates has been normalized with respect to the free-molecular heat flux<sup>53,54</sup>

$$q_x = \rho_m \sqrt{\frac{RT_m}{2\pi}} \left( c_v + \frac{1}{2}R \right) (T_U - T_L), \quad (50)$$

where  $\rho_m$  is the density of the gas midway between the plates,  $R$  is the specific gas constant, and  $c_v$  is the heat capacity at constant volume. The results are compared to the free-molecular solution, the continuum NSF solution, and the NSF solution with temperature jump boundary conditions. The temperature jump distance,  $g$ , is found as<sup>53</sup>

$$g = \frac{2 - \mathcal{A}}{\mathcal{A}} (2\pi RT)^{\frac{1}{2}} \frac{K}{(\gamma + 1) c_p p}, \quad (51)$$

where  $K$  is the thermal conductivity. In order to stay consistent with the BGK approximation the thermal conductivity is taken to be  $K = c_p \mu$ , where  $c_p$  is the heat capacity at constant pressure, thus ensuring a Prandtl number of unity. The temperature directly adjacent to the wall is then found as,

$$T = g \frac{\partial T}{\partial y} + T_w, \quad (52)$$

which is used as the temperature boundary condition in the NSF equations.

The performance of the NKS and semi-implicit schemes have been compared in Figure 8. The L2-norm values are with respect to the density and are normalized by the residual value of the first iteration. The semi-implicit solver uses a CFL number of 0.5. The NKS solver continues to outperform the semi-implicit scheme, in fact even more so than in the Couette flow case. Savings in CPU time of between 8 and 15 times were found for the cases considered. This improved performance is expected since it was found that the maximum wave speed of the system increases as the heat flux increases, see Figure 3. It is also found that the convergence stalls earlier for the Kn=0.1 and Kn=1 cases when solved using the semi-implicit scheme.

Although promising results have been found for temperature slip and heat flux between the plates there are still some issues with this case. It was found that the temperature in the middle of the plates drifted from the expected value of 397.37 K. This phenomena can be observed in Figure 9 (a) which displays the temperature distributions between the plates at several Knudsen numbers. The heat flux between the plates

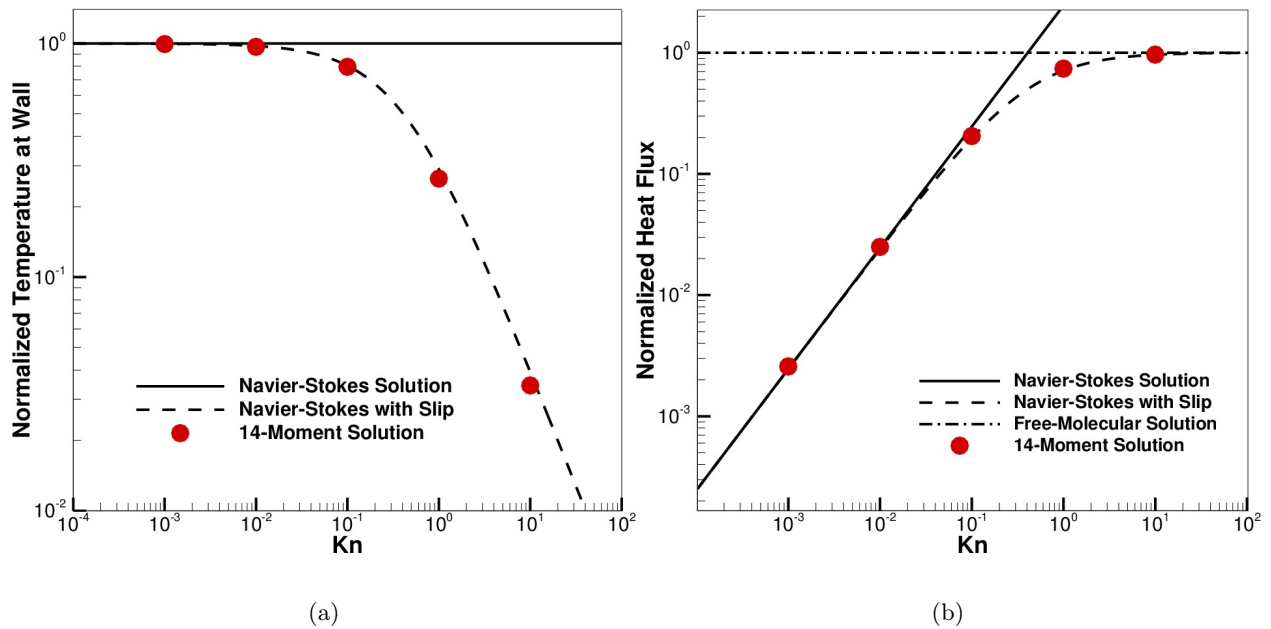


Figure 7: (a) Normalized temperature at the wall with respect to Knudsen number. (b) Heat flux between the plates, normalized with respect to the free-molecular value, as a function of Knudsen number.

has also been considered in Figure 9 (b). Steep changes in the heat flux are observed adjacent to either wall, which is in contrast to the expected constant heat flux. This implies an inaccuracy of the boundary condition, and also lead to the discrepancy between the top and bottom plate temperatures which was mentioned above. Similar inaccuracies have also been observed in previous studies of moment closures applied to heat transfer problems using a solid-wall half-Maxwellian boundary condition.<sup>55</sup>

In conclusion, the results found show potential for the 14-moment closure's ability to model heat transfer. The normalized temperature results, Figure 7(a), display the expected temperature jump, beginning in the transition region, and the values are in close agreement with those predicted by the NSF solution with slip-temperature boundary conditions. The results for normalized heat flux, Figure 7(b), are also consistent with the NSF solution with slip-temperature boundary conditions. Some intangible results are found for the heat flux and temperature distributions. However, it is suspected that these can be mitigated by implementing a more carefully formulated boundary condition, such as the modification to the solid-wall half-Maxwellian boundary conditions considered by Struchtrup.<sup>56</sup>

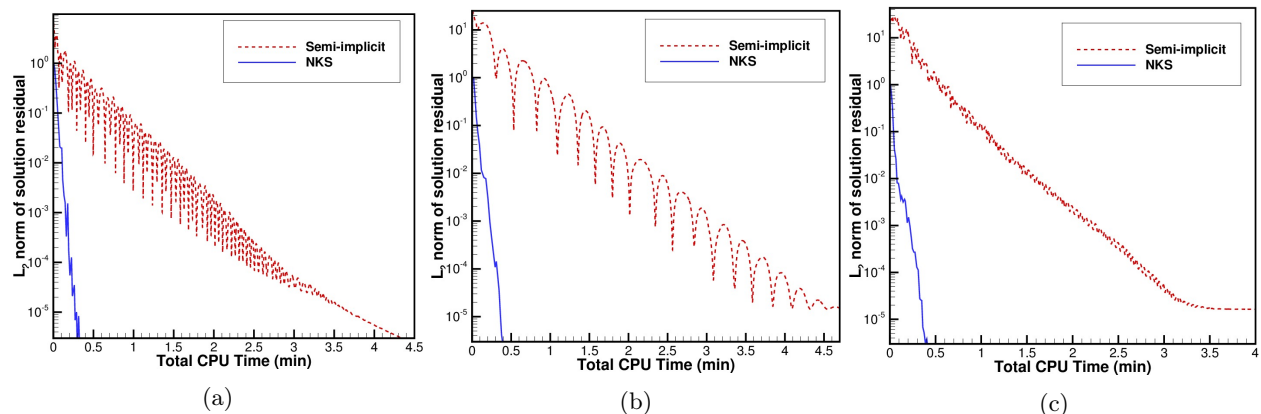


Figure 8: Comparison of convergence of the solution residuals for the NKS and semi-implicit solvers when applied to a heated flat plates case with a Knudsen number of (a) 0.01, (b) 0.1, and (c) 1.

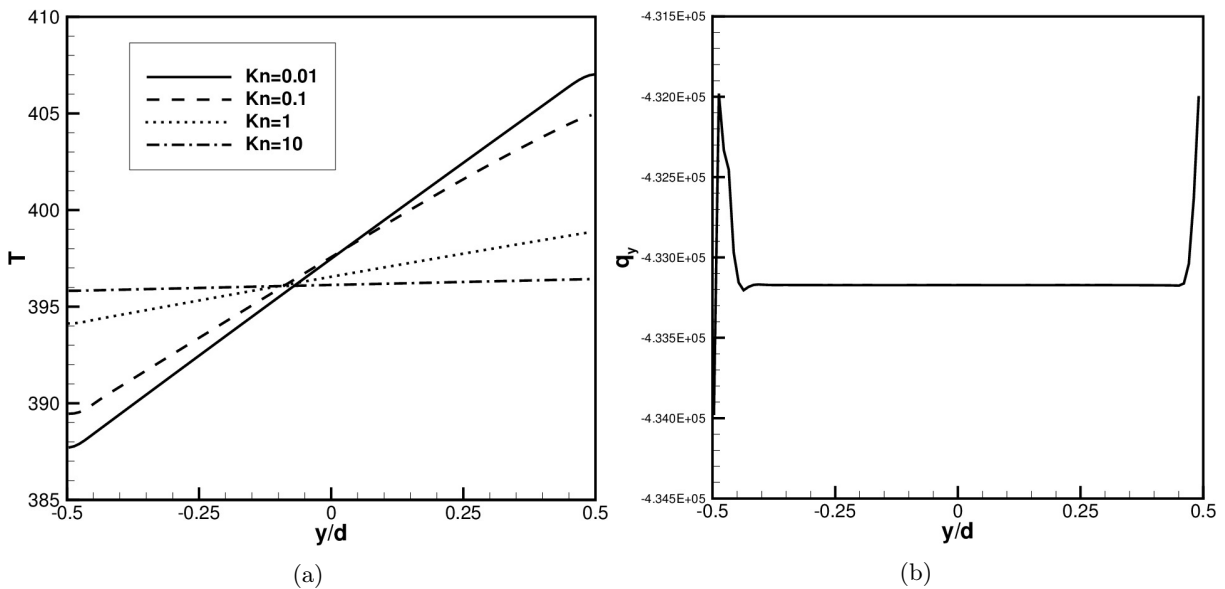


Figure 9: (a) Temperature distributions between heated plates. (b) Heat flux between heated plates at  $Kn=1$ .

#### V.D. Subsonic Flow Past a Circular Cylinder

Subsonic flow past a circular cylinder is considered for several Knudsen numbers spanning the continuum and transition regimes. For comparison, simulations were also executed using the Gaussian<sup>8,27</sup> and regularized Gaussian<sup>8,28</sup> closures. Recall that the Gaussian closure is a 10-moment maximum-entropy closure. The regularized Gaussian closure is an extension of the Gaussian closure which incorporates anisotropic thermal-diffusion effects using added elliptic terms. For all cases the gas considered is argon at standard atmospheric density and pressure of  $1.225 \text{ kg/m}^3$  and  $101.325 \text{ kPa}$ , respectively, and a temperature of  $397.37 \text{ K}$ . Solutions were found using each closure technique on a quadrilateral, body fitted, computational mesh of between 16 640 and 32 000 cells. The mesh was stretched resulting in a much greater concentration of cells near the cylinder surface. These mesh sizes were chosen based on past studies by McDonald<sup>30</sup> and Lam<sup>32</sup> and a mesh refinement study, the results of which are summarized in Figure 10. Speed ratios,  $S$ , considered were 0.027 and 0.107, corresponding to mach numbers of 0.0296 and 0.117, respectively. The speed ratio is defined as the ratio between the free stream gas speed and the most probable particle speed. The temperature of the cylinder was set equivalent to the free-stream gas temperature of  $397.37 \text{ K}$ . The solid-wall half-Maxwellian boundary conditions, with an accommodation coefficient of  $\mathcal{A} = 1$ , were used at the cylinder edge.

This section begins with comparisons of various gas property contours at  $Kn=0.01$  and 1, found using the 14-moment, Gaussian, and regularized Gaussian closures. Various important non-equilibrium flow features and discrepancies amongst the solvers are noted. A more quantitative result is then presented by considering the coefficient of drag of the cylinder. Finally, the solution convergence of the NKS and semi-implicit solvers are compared for several cases.

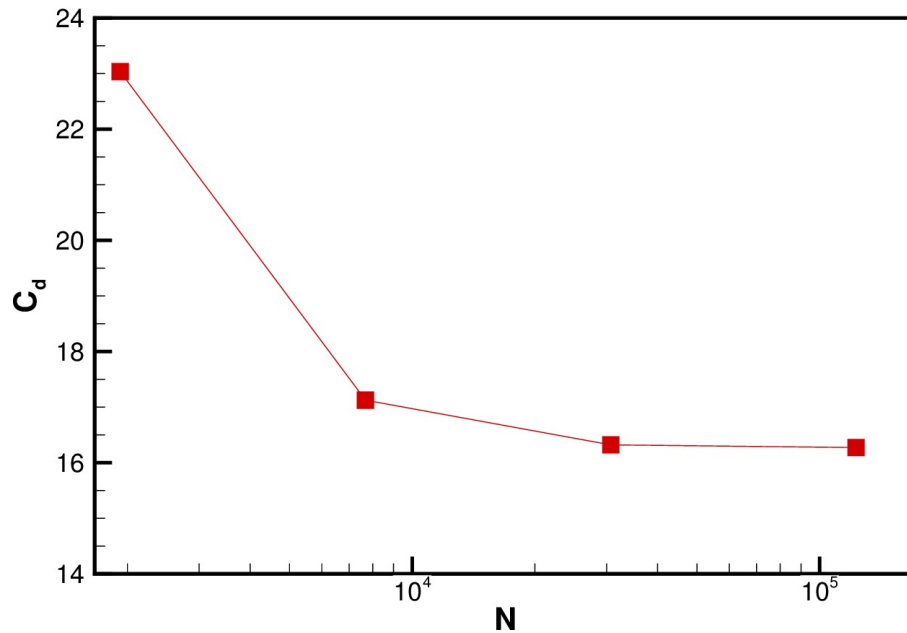


Figure 10: Mesh refinement study for subsonic flow around a circular cylinder at  $Kn=0.1$  and  $S=0.027$ .  $N$  is the total number of computational cells.

#### V.D.1. Results for $Kn=0.002$ and $S=0.027$

Solutions found for the continuum case,  $Kn = 0.002$ , are presented in Figures 11 and 12. For this case the Reynolds number is 24.3728. It can be seen that the Mach number contours are very similar for each of the solution methods, as is expected. Since this case is in the continuum regime, negligible velocity slip is observed at the surface of the cylinder. The velocity streamlines show the formation of a recirculation region downstream of the cylinder. This is a well established phenomena at the Reynolds number considered. The gas is close to local thermodynamic equilibrium for this low Knudsen number case, and therefore the variations in temperature are small, however the Gaussian solution shows slightly higher temperatures near the cylinder, signifying that even for this continuum regime case heat transfer is starting to have an effect. The regularized Gaussian and 14-moment closure solutions are in good agreement. The temperature field for both solution methods is overall uniform, with very slight heating in front and downstream of the cylinder. This case is a good verification of the 14-moment closure's predictive ability for continuum regime flows in two-dimensions.

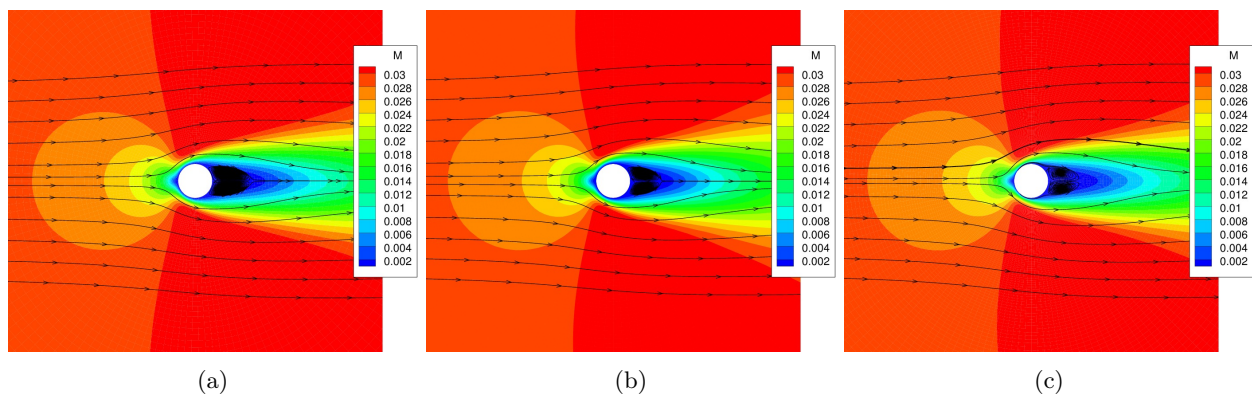


Figure 11: Mach number contours and velocity streamlines for subsonic flow past a circular cylinder at  $Kn = 0.002$  found by solving the (a) Gaussian, (b) regularized Gaussian, and (c) 14-moment closures.

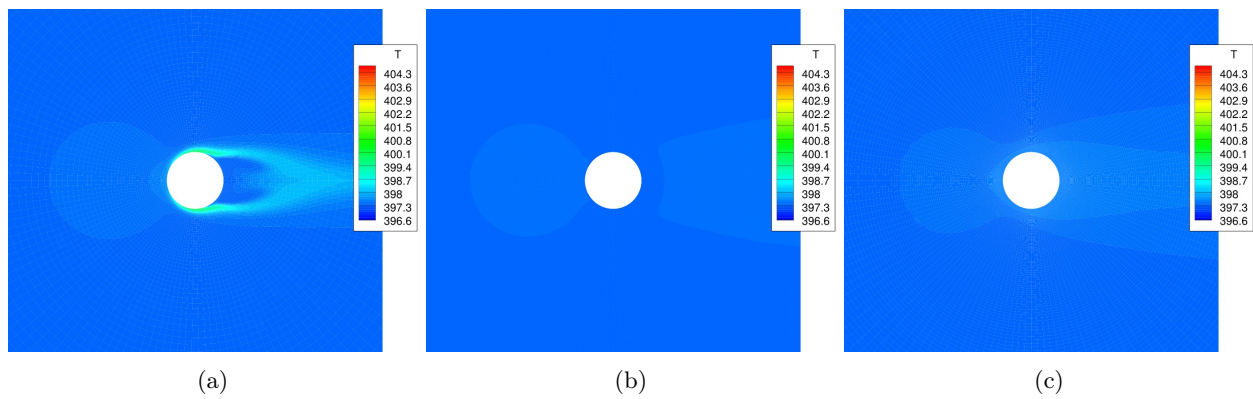


Figure 12: *Temperature contours for subsonic flow past a circular cylinder at  $Kn = 0.002$  found by solving the (a) Gaussian, (b) regularized Gaussian, and (c) 14-moment closures.*

#### V.D.2. Results for $Kn=1$ and $S=0.027$

Solutions found for the transition-regime case,  $Kn = 1$ , are presented in Figures 13, 14, and 15. For this case the Reynolds number is 0.0487. It can be observed that the Mach number contours now show discrepancy between the closure techniques, although all show significant slip, as expected. The recirculation region observed in the continuum regime has disappeared, as would be anticipated for this much lower Reynolds number. The boundary layer thickness relative to the cylinder diameter has also increased, which is expected from kinetic theory. The Gaussian solution shows very significant localized heating when compared with the regularized Gaussian and 14-moment closures. This is anticipated as the Gaussian solution does not consider heat transfer, which is significant in this regime. The heat-flux streamlines (Figure 15) are similar for the regularized Gaussian and 14-moment solutions, however the temperature contours differ. The regularized Gaussian shows a decrease in temperature in front of the cylinder and increased temperature behind, whereas the opposite is true for the 14-moment closure. Therefore, the heat flux in the 14-moment solution is oriented in the opposite direction to that expected by modelling based on the temperature gradient. This so called temperature polarization and non-gradient transport effect have been previously observed when considering flows in the transition regime, such as in analytical solutions for flow around a sphere by Torrilhon.<sup>57</sup> The 14-moment closure's ability to predict this non-equilibrium phenomena is very promising.

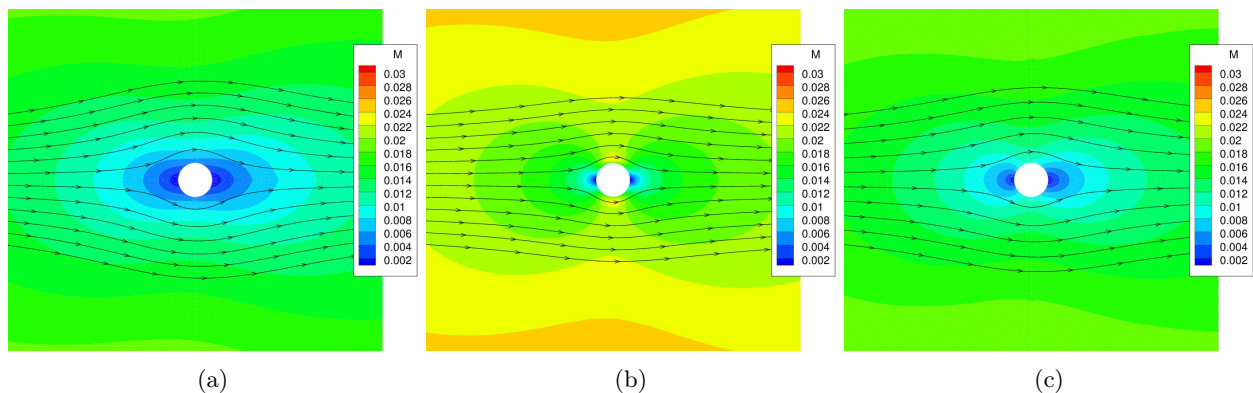


Figure 13: *Mach number contours and velocity streamlines for subsonic flow past a circular cylinder at  $Kn = 1$  found by solving the (a) Gaussian, (b) regularized Gaussian, and (c) 14-moment closures.*

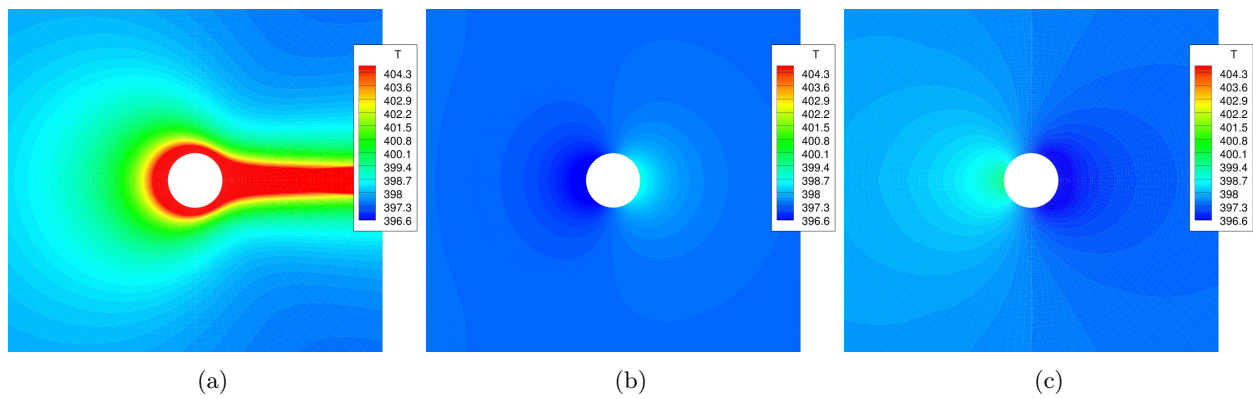


Figure 14: Temperature contours for subsonic flow past a circular cylinder at  $Kn = 1$  found by solving the (a) Gaussian, (b) regularized Gaussian, and (c) 14-moment closures.

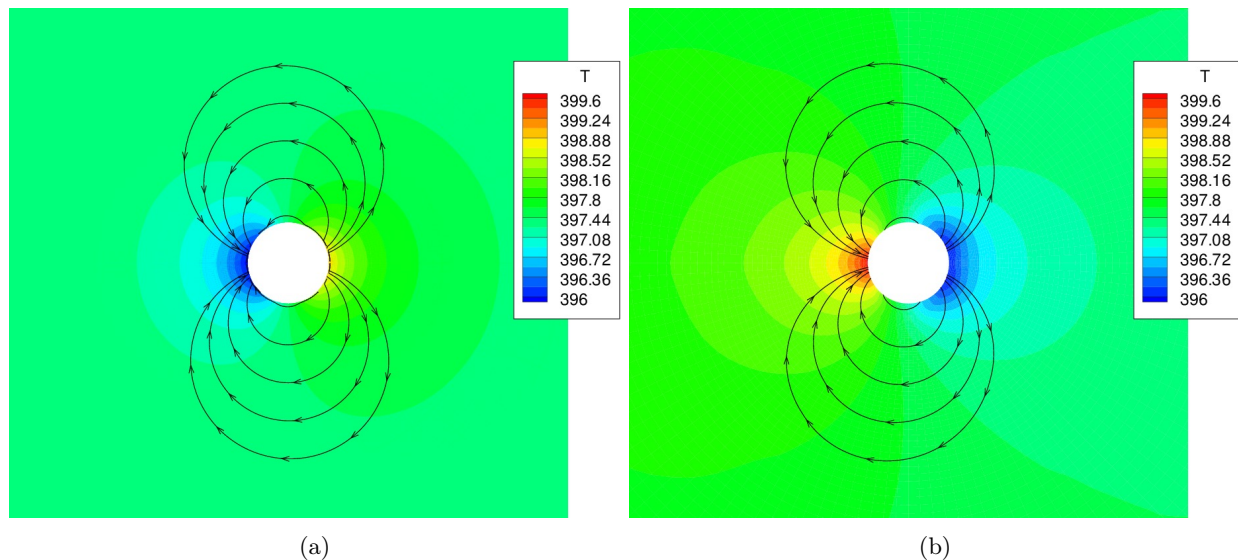


Figure 15: Temperature contours and heat-flux streamlines for subsonic flow past a circular cylinder at  $Kn = 1$  found by solving the (a) regularized Gaussian and (b) 14-moment closures. Note that the temperature contours have been rescaled to show more detail.

### V.D.3. Drag Prediction

The predicted values of the drag coefficient,  $c_d$ , are also considered for the 14-moment and Gaussian closures. These results are compared with experimental values found by Coudeville *et al.*<sup>58</sup> Although these experimental values were found for air, they are expected to be very similar to those of argon due to their similar viscosity, and are therefore still used for comparison, particularly to get an idea of the trends of the drag coefficient into the free-molecular regime. Furthermore, when these cases were run for both air and argon using the Gaussian closure the drag value was found not to change significantly. The values of drag coefficient are in excellent agreement with those of the Gaussian closure for the lower Knudsen number cases of  $Kn=0.01$  and  $Kn=0.1$ . This is expected since the contributions of heat transfer are small and, as seen in the results presented in Section V.D.1, the solutions are very similar. As the free-molecular regime is approached the predicted drag coefficients for the closure methods begin to diverge. However, the 14-moment closure seems to follow the trends of the experimental solution more closely than the Gaussian closure. This is expected since the 14-moment closure considers a higher number of moments, and thus should remain valid to a higher Knudsen number. These results are promising as they not only validate the 14-moment closure at the beginning of the transition regime, but also show its improved predictive capabilities at higher Knudsen numbers.

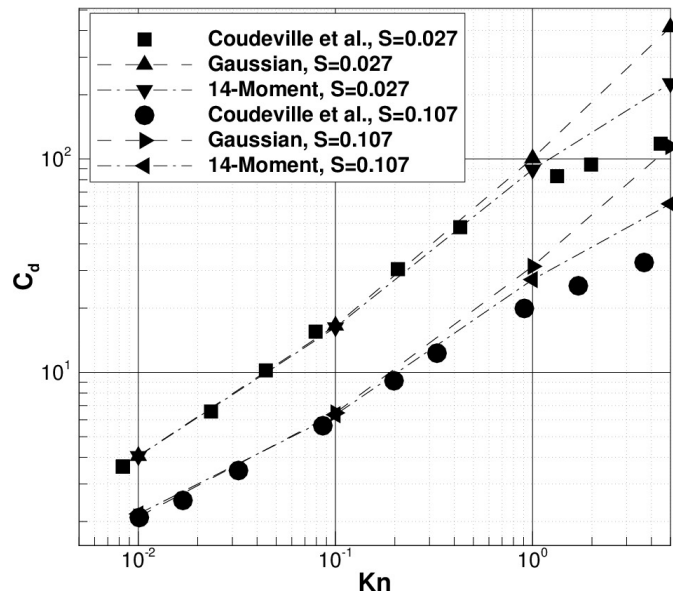


Figure 16: Comparison of predicted drag coefficients found using the 14-moment and Gaussian closures and experimental values for air found by Coudeville et al..

Finally, a comparison of solution convergence histories are considered for the NKS and semi-implicit solvers. The semi-implicit solver uses a CFL number of 0.15-0.3 depending on the Knudsen number (higher Knudsen number cases require lower CFL numbers). The NKS solver is found to continue to offer significant gains in computation speed, with a factor of at least 2.5 times saving in CPU time. Furthermore, the NKS solver is less prone to convergence stall than the semi-implicit scheme.

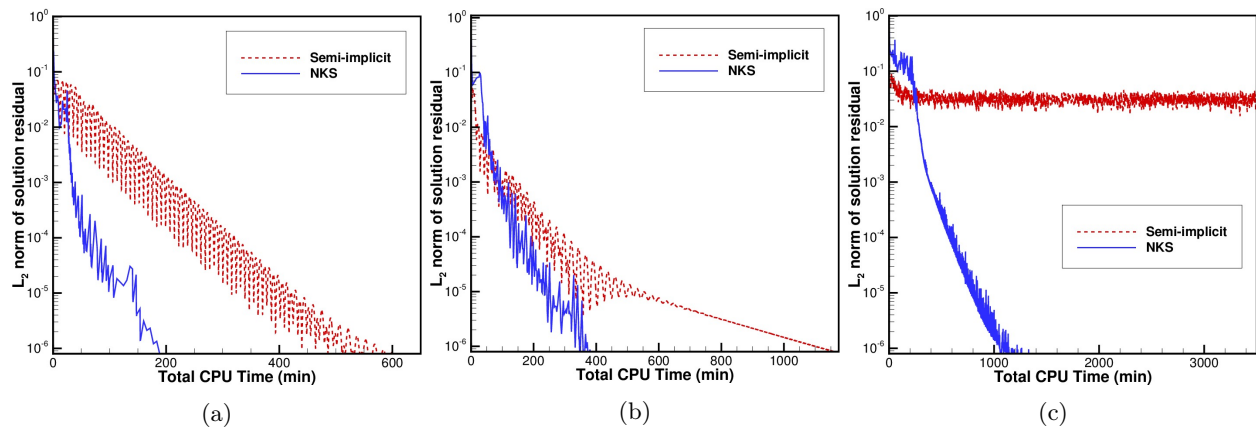


Figure 17: Comparison of solution convergence using the NKS and semi-implicit schemes for the circular cylinder case with a Knudsen number of (a) 0.01, (b) 0.1, and (c) 1 and a speed ratio of  $S=0.027$ .

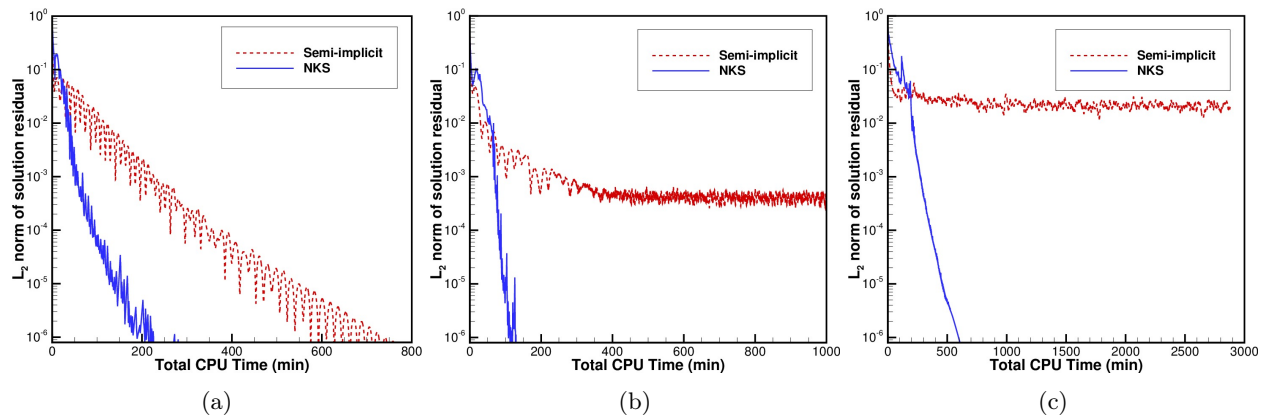


Figure 18: Comparison of solution convergence using the NKS and semi-implicit schemes for the circular cylinder case with a Knudsen number of (a) 0.01, (b) 0.1, and (c) 1 and a speed ratio of  $S=0.107$ .

### V.E. Lid-Driven Cavity Flow

The final case considered is lid-driven cavity flow. A square computational domain of  $150 \times 150$  Cartesian cells, for a total of 22 500 cells, with three stationary solid walls and one moving wall with a tangential x-direction velocity,  $U = 50$  m/s, is utilized (see Figure 19). The square cavity contains argon with an initial pressure of 101.325 kPa and temperature of 273 K. The wall temperatures,  $T_w$ , are set equivalent to the internal gas, i.e.  $T_w = 273$  K. The residuals for this case are reduced by at least four orders of magnitude.

Solutions are found at  $Kn=0.001$ ,  $Kn=0.05$  and  $Kn=0.1$ . These results are compared to results found using the regularized Gaussian closure,<sup>32</sup> as well as solutions found using the NSF equations for the continuum case, and a DSMC solution found by John, Gu, and Emerson<sup>59,60</sup> for the transition regime cases. The DSMC method is considered to be accurate in the transition regime, however due to its particle nature is very computationally intensive. In the DSMC study a variable hard sphere collision model is used, this leads to some discrepancy with the 14-moment results since they employed the BGK collision model. In the DSMC cases the Knudsen number is adjusted by varying the reference pressure, however for the 14-moment closure, regularized Gaussian, and NSF solutions the geometry of the cavity was adjusted instead. To stay consistent with the DSMC study the mean free path,  $\Lambda$ , is now found as

$$\Lambda = \frac{\mu}{p} \sqrt{\frac{\pi RT}{2}}. \quad (53)$$

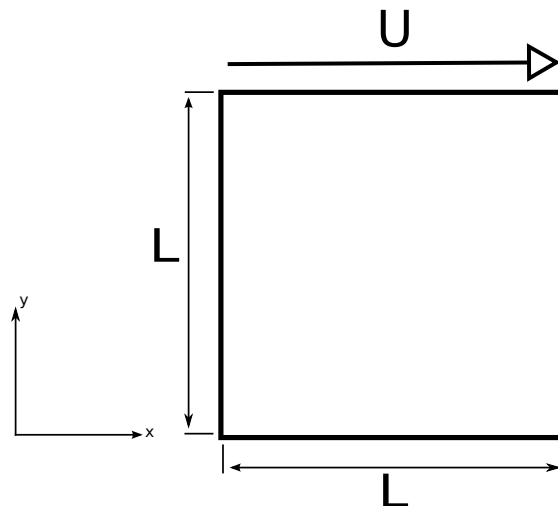


Figure 19: Schematic of the lid-driven cavity.

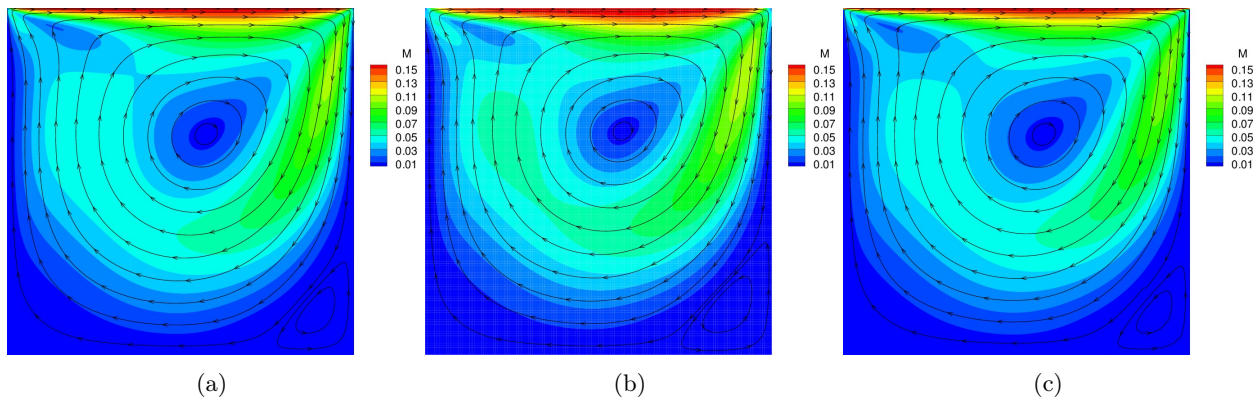


Figure 20: Mach number contours for lid-driven cavity flow at  $Kn = 0.001$  found using the (a) regularized Gaussian closure, (b) 14-moment closure, and (c) NSF equations.

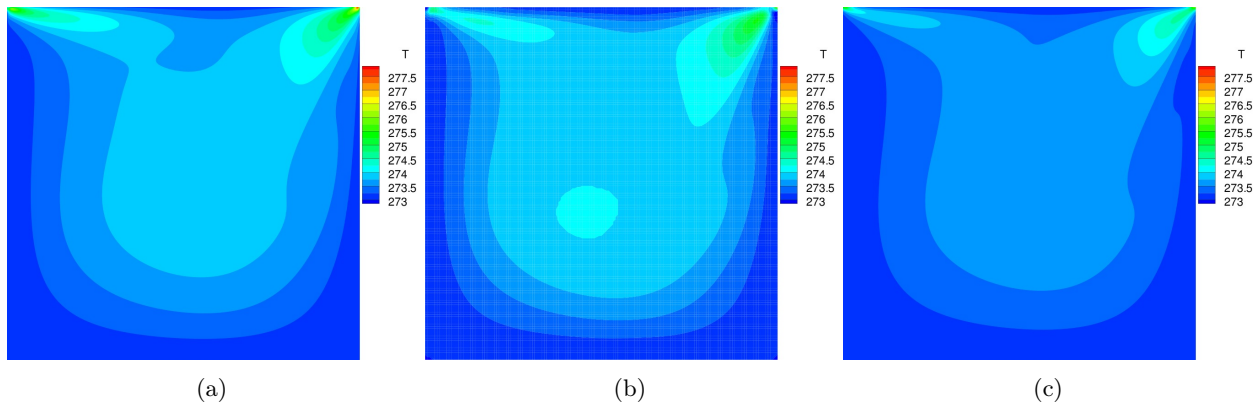


Figure 21: Temperature contours for lid-driven cavity flow at  $Kn = 0.001$  found using the (a) regularized Gaussian closure, (b) 14-moment closure, and (c) NSF equations.

### V.E.1. Results for $Kn=0.001$

The resulting Mach number and temperature profiles for this case can be seen in Figures 20 and 21. The solutions found using the regularized Gaussian closure, 14-moment closure, and NSF equations are compared. The Mach number contours and velocity stream lines show good agreement for all three methods as expected. The temperature profiles are also in fair agreement for each solution technique, showing an overall uniform temperature distribution as expected in this regime. However, the regularized Gaussian and 14-moment closures result in slightly higher temperatures overall.

### V.E.2. Results for $Kn=0.05$

Results at  $Kn=0.05$  are now considered. Plots comparing Mach number, shear stress, and temperature contours can be found in Figures 22, 23, and 24, respectively. Since heat flux is no longer negligible at this Knudsen number, the heat-flux streamlines are now overlaid on the temperature contours. The Mach number contours all display velocity slip at the lid as anticipated, however the slip seems to be slightly overpredicted in the regularized Gaussian solution. Furthermore, the regularized Gaussian overpredicts the slip at the top of the left and right walls when compared to the DSMC solution. It is clear that the 14-moment solution is in better agreement with the DSMC result's Mach number contours. Shear stress now becomes significant, especially adjacent to the moving lid, as seen in Figure 23. All three solution techniques show fair agreement, but the 14-moment solution is closer to the DSMC result than the regularized Gaussian. Both the 14-moment closure and DSMC method predict a hot region in the top right corner, and a cold region in the top left corner, however the absolute temperature values are much larger for the 14-moment results. This cold region is a consequence of expansion cooling and the hot region results from viscous heating.<sup>59,60</sup>

The regularized Gaussian closure predicts both a hot and cold spot in each corner. The heat-flux streamlines show discrepancies between all three methods, especially in the lower half of the cavity. However, in the top half of the cavity, where heat transfer is most significant, the heat flux lines for each method show a similar left to right trend. Interestingly, both the 14-moment closure technique and DSMC method predict a counter-gradient heat flux, whereas the regularized Gaussian closure does not. A similar result was observed for the circular cylinder case (see Figure 15).

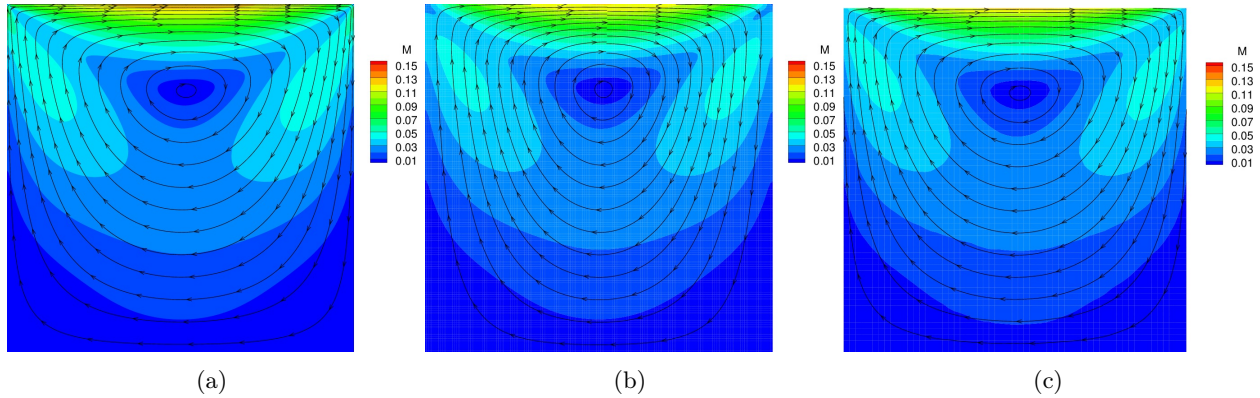


Figure 22: Mach number contours for lid-driven cavity flow at  $Kn = 0.05$  found using the (a) regularized Gaussian closure, (b) 14-moment closure, and (c) DSMC technique.<sup>59,60</sup>

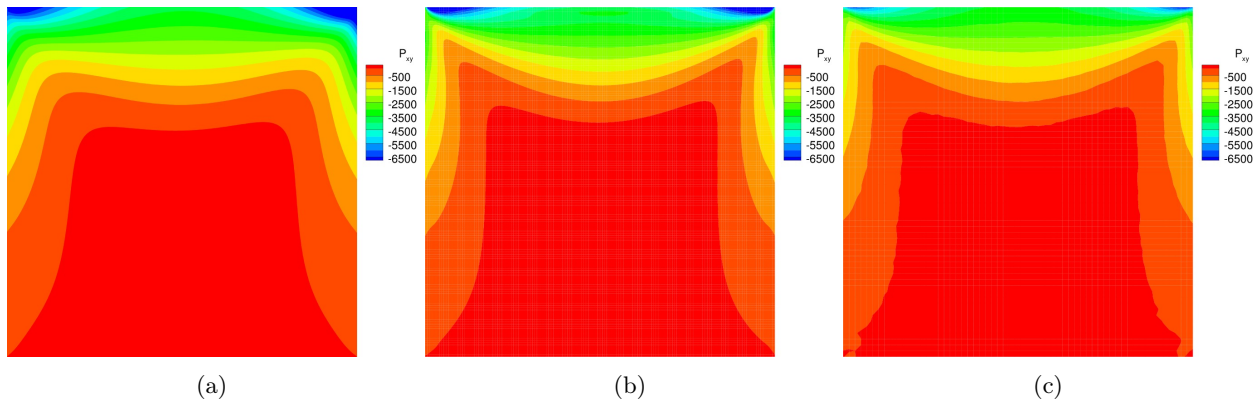


Figure 23: Shear stress contours for lid-driven cavity flow at  $Kn = 0.05$  found using the (a) regularized Gaussian closure, (b) 14-moment closure, and (c) DSMC technique.<sup>59,60</sup>

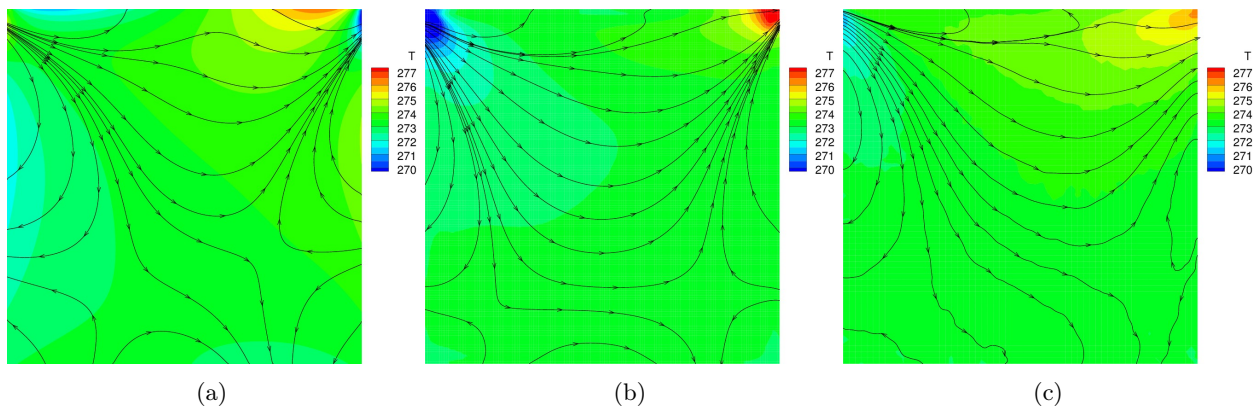


Figure 24: Temperature contours and heat-flux streamlines for lid-driven cavity flow at  $Kn = 0.05$  found using the (a) regularized Gaussian closure, (b) 14-moment closure, and (c) DSMC technique.<sup>59,60</sup>

V.E.3. Results for  $Kn=0.1$

Finally, a transition-regime case at  $Kn=0.1$  is considered (Figures 25, 26, and 27). The conclusions drawn from the  $Kn=0.05$  case continue to apply. The regularized Gaussian closure continues to slightly overpredict slip in the top corners, as seen in Figure 25. The 14-moment closure's prediction of shear stress continues to be in closer agreement with the DSMC results than the regularized Gaussian, however its prediction is now considerably worse than at  $Kn=0.05$ . At this higher Knudsen number the hot and cold spots have increased in size in the 14-moment and DSMC solutions. The 14-moment closure continues to overpredict the absolute temperatures in the top corners, and the counter-gradient heat flux is present in the both 14-moment and DSMC results, but absent from the regularized Gaussian results.

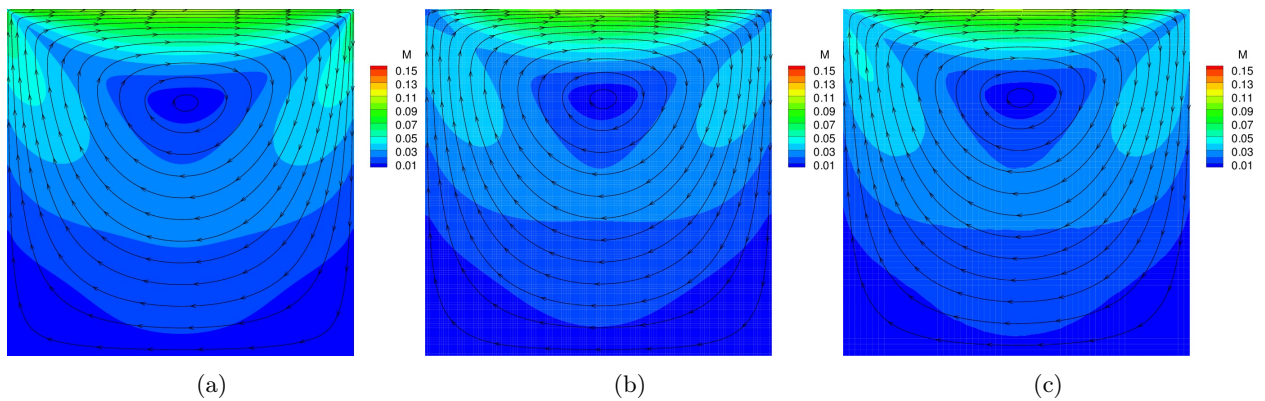


Figure 25: Mach number contours for lid-driven cavity flow at  $Kn = 0.1$  found using the (a) regularized Gaussian closure, (b) 14-moment closure, and (c) DSMC technique.<sup>59,60</sup>

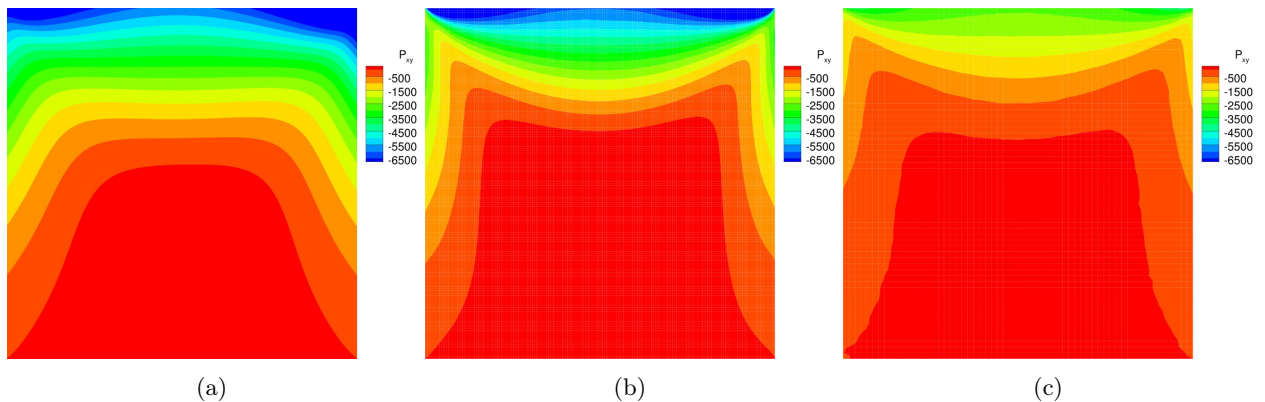


Figure 26: Shear stress contours for lid-driven cavity flow at  $Kn = 0.1$  found using the (a) regularized Gaussian closure, (b) 14-moment closure, and (c) DSMC technique.<sup>59,60</sup>

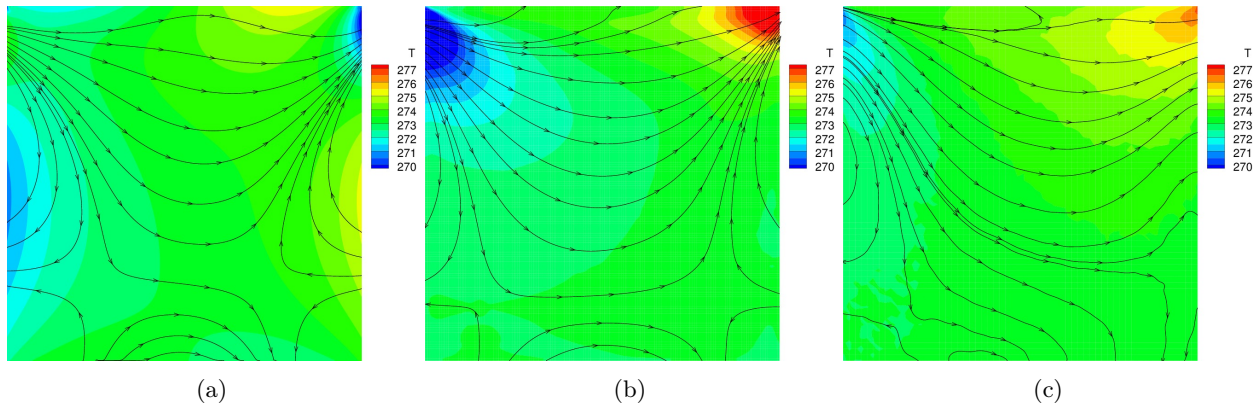


Figure 27: *Temperature contours and heat-flux streamlines for lid-driven cavity flow at  $Kn = 0.1$  found using the (a) regularized Gaussian closure, (b) 14-moment closure, and (c) DSMC technique.*<sup>59, 60</sup>

## VI. Conclusion and Future Work

A new, 14-moment, maximum-entropy-based, interpolative closure has been investigated and employed to solve a variety of canonical two-dimensional flow problems. A dispersion analysis of the 14-moment closure system has been presented which verifies the systems stability as well as demonstrating its potential to be applied to high mach number flows, through its high frozen wave speeds near the Junk subspace. This analysis also motivated the exploration of an implicit solver due to its prediction of large wave speeds for near-equilibrium flows.

Two-dimensional solutions to this new closure have been obtained for a planar Couette flow, conduction between heated flat plates, subsonic flow past a circular cylinder, and lid-driven cavity flow. In order to consider these cases, valid boundary conditions, which reproduce non-equilibrium phenomena, were developed based on the solid-wall half-Maxwellian boundary condition. The Couette-flow results for normalized velocity and shear stress were found to be in excellent agreement with both the well established Gaussian closure and the analytical solution of Lees. The case of conduction between two heated plates was also found to be in good agreement with the expected result found using the NSF equations with temperature jump boundary conditions. The results for subsonic flow around a circular cylinder showed expected behaviours such as velocity slip and an increase in boundary layer thickness with increasing Knudsen number. The solutions found in the continuum regime were in good agreement with the well established regularized Gaussian closure, and the results found in the transition regime displayed temperature polarization and non-gradient transport. These results also showed an improved prediction of drag for high Knudsen number flows, relative to the 10-moment Gaussian closure. The lid-driven cavity flow results were compared to those of the NSF equations, regularized Gaussian closure, and DSMC technique. The 14-moment closure was found to be in better agreement with the DSMC technique in the transition regime than the regularized Gaussian closure. The 14-moment closure was successful in predicting the presence of expansion cooling and viscous heating, as well as a counter-gradient heat flux, which is also seen in the DSMC results. In conclusion, the 14-moment closure showed improvements over the 10-moment Gaussian closure, as would be expected since more moments are considered. Furthermore, it was able to predict a counter-gradient heat flux, which was not possible using the regularized Gaussian closure.

Finally, compared to the semi-implicit approach, the use of an implicit NKS solver was found to significantly decrease the computational cost of obtaining solutions for the 14-moment closure. The savings were between 2 and 15 times, depending on the problem. Additionally, based on the preliminary results found using a simplified analytic Jacobian, which were described in Section IV.C, it is expected that an additional savings of 2-3 times could be achieved by implementing a general non-finite-difference procedure for finding the Jacobians. This would lead to a factor of savings on the order of 30 times compared to the semi-implicit approach. The NKS solver was also able to obtain converged solutions for cases where the semi-implicit method stalled. The effectiveness of the solver was found to be consistent with the conclusions about the maximum wave speeds and stiffness of the system predicted by the dispersion analysis.

Although the study presented has been successful in many respects, there is still further development required for this novel 14-moment closure. The equation system and numerical solver should be extended to

handle three-dimensional flows of both monatomic and diatomic gases. It is clear that the chosen boundary condition technique has some issues, such as those seen in the heat transfer between flat plates cases. This boundary condition should be reconsidered and possible modifications which mitigate these issues should be explored. The computational cost of the NKS method could be improved by implementing a more accurate method of calculating the required Jacobians, such as algebraic formulations. Based on findings for a simplified analytic flux-Jacobian in the continuum regime, it is expected that a general analytic form of the flux-Jacobian will greatly improve the computational time required to find solutions. However, due to the complexity of the system a feasible form of this Jacobian will not be trivial, and clever algebraic and physical simplifications or assumptions may be necessary.

## Acknowledgments

Computational resources were provided by the SciNet High Performance Computing Consortium at the University of Toronto and Computer/Calcul Canada through funding from the Canada Foundation for Innovation (CFI) and the Province of Ontario, Canada. The authors would like to thank Christopher Lam for his assistance in generating the regularized Gaussian solutions and helpful discussions. B. R. Tensuda also acknowledges the Province of Ontario for their support through an Ontario Graduate Scholarship. The authors thank David R. Emerson, Benzi John, and Xiao-Jun Gu at STFC Daresbury Laboratory for providing the lid driven cavity flow DSMC data.

## References

- <sup>1</sup>Shen, C., *Rarefied Gas Dynamics: Fundamentals, Simulations and Micro Flows*, Springer, New York, 2010.
- <sup>2</sup>Ho, C. and Tai, Y., "Micro-Electro-Mechanical-Systems (MEMS) and Fluid Flows," *Ann. Rev. Fluid Mech.*, Vol. 30, 1998, pp. 579–612.
- <sup>3</sup>Nie, X., Doolen, G. D., and Chen, S., "Lattice-Boltzmann Simulations of Fluid Flows in MEMS," *J. Comput. Phys.*, Vol. 107, 2002, pp. 279–289.
- <sup>4</sup>Sherman, F. S. and Talbot, L., "Experiment Versus Kinetic Theory for Rarefied Gases," *Rarefied Gas Dynamics*, edited by F. M. Devienne, Vol. 3 of *International Series on Aeronautical Sciences and Space Flight*, Pergamon Press, New York, 1960, pp. 161–191.
- <sup>5</sup>Chu, C., "Kinetic Theoretic Description of the Formation of a Shock Wave," *Phys. Fluids*, Vol. 8, No. 1, 1965, pp. 12–22.
- <sup>6</sup>Bird, G. A., *Molecular Gas Dynamics and the Direct Simulation of Gas Flows*, Clarendon Press, Oxford, 1994.
- <sup>7</sup>Mieussens, L., "Discrete Velocity Model and Implicit Scheme for the BGK Equation of Rarefied Gas Dynamics," *Mathematical Models and Methods in Applied Sciences*, Vol. 10, No. 8, 2000, pp. 1121–1149.
- <sup>8</sup>Groth, C. P. T. and McDonald, J. G., "Towards Physically-Realizable and Hyperbolic Moment Closures for Kinetic Theory," *Continuum Mech. Thermodyn.*, Vol. 21, No. 6, 2009, pp. 467–493.
- <sup>9</sup>Levermore, C. D., "Moment Closure Hierarchies for Kinetic Theories," *J. Stat. Phys.*, Vol. 83, 1996, pp. 1021–1065.
- <sup>10</sup>Müller, I. and Ruggeri, T., *Rational Extended Thermodynamics*, Springer-Verlag, New York, 1998.
- <sup>11</sup>McDonald, J. G., Sachdev, J. S., and Groth, C. P. T., "Application of Gaussian Moment Closure to Micro-Scale Flows with Moving and Embedded Boundaries," *AIAA J.*, Vol. 52, No. 9, 2014, pp. 1839–1857.
- <sup>12</sup>McDonald, J. G. and Torrilhon, M., "Affordable Robust Moment Closures for CFD Based on the Maximum-Entropy Hierarchy," *J. Comput. Phys.*, Vol. 251, 2013, pp. 500–523.
- <sup>13</sup>Maxwell, J. C., "On the Dynamical Theory of Gases," *Philosophical Transactions of the Royal Society of London*, Vol. 157, 1867, pp. 49–88.
- <sup>14</sup>Boltzmann, L., "Weitere Studien über das Wärmegleichgewicht unter Gasmolekülen," *Sitz. Math.-Naturwiss. Cl. Akad. Wiss. Wien*, Vol. 66, 1872, pp. 275–370.
- <sup>15</sup>Gombosi, T. I., *Gaskinetic Theory*, Cambridge University Press, Cambridge, 1994.
- <sup>16</sup>Patterson, G. N., *Introduction to the Kinetic Theory of Gas Flows*, University of Toronto Press, Toronto, 1961.
- <sup>17</sup>Present, R. D., *Kinetic Theory of Gases*, McGraw-Hill, New York, 1958.
- <sup>18</sup>Bhatnagar, P. L., Gross, E. P., and Krook, M., "A Model for Collision Processes in Gases. I. Small Amplitude Processes in Charged and Neutral One-Component Systems," *Physical Rev.*, Vol. 94, No. 3, 1954, pp. 511–525.
- <sup>19</sup>Patterson, G. N., *Molecular Nature of Aerodynamics*, University of Toronto Press, Toronto, 1981.
- <sup>20</sup>Grad, H., "On the Kinetic Theory of Rarefied Gases," *Commun. Pure Appl. Math.*, Vol. 2, 1949, pp. 331–407.
- <sup>21</sup>Chapman, S., "On the Kinetic Theory of a Gas. Part II. – A Composite Monoatomic Gas: Diffusion, Viscosity, and Thermal Conduction," *Phil. Trans. Royal Soc. London A*, Vol. 217, 1916, pp. 115–116.
- <sup>22</sup>Enskog, D., *Kinetische Theorie der Vorgänge in Massing Verdumten Gasen*, Ph.D. thesis, University of Upsala, 1917.
- <sup>23</sup>McDonald, J. G. and Groth, C. P. T., "Towards Realizable Hyperbolic Moment Closures for Viscous Heat-Conducting Gas Flows Based on a Maximum-Entropy Distribution," *Continuum Mech. Thermodyn.*, Vol. 25, No. 5, 2013, pp. 573–603.
- <sup>24</sup>Hamburger, H. L., "Hermitian Transformations of Deficiency-Index (1, 1), Jacobian Matrices, and Undetermined Moment Problems," *Amer. J. Math.*, Vol. 66, 1944, pp. 489–552.

- <sup>25</sup>Levermore, C. D. and Morokoff, W. J., “The Gaussian Moment Closure for Gas Dynamics,” *SIAM J. Appl. Math.*, Vol. 59, No. 1, 1998, pp. 72–96.
- <sup>26</sup>Brown, S. L., Roe, P. L., and Groth, C. P. T., “Numerical Solution of a 10-Moment Model for Nonequilibrium Gasdynamics,” Paper 95-1677, AIAA, June 1995.
- <sup>27</sup>McDonald, J. G. and Groth, C. P. T., “Numerical Modeling of Micron-Scale Flows Using the Gaussian Moment Closure,” Paper 2005-5035, AIAA, June 2005.
- <sup>28</sup>McDonald, J. G. and Groth, C. P. T., “Extended Fluid-Dynamic Model for Micron-Scale Flows Based on Gaussian Moment Closure,” Paper 2008-0691, AIAA, January 2008.
- <sup>29</sup>Junk, M., “Domain of Definition of Levermore’s Five-Moment System,” *J. Stat. Phys.*, Vol. 93, No. 5/6, 1998, pp. 1143–1167.
- <sup>30</sup>McDonald, J. G., *Extended Fluid-Dynamic Modelling for Numerical Solution of Micro-Scale Flows*, Ph.D. thesis, University of Toronto, October 2010.
- <sup>31</sup>Tensuda, B., McDonald, J., and Groth, C., “Numerical Solution of a Maximum-Entropy-Based 14-Moment Closure for Multi-Dimensional Flows,” *Proceedings of the Eighth International Conference on Computational Fluid Dynamics, ICCFD8, Chengdu, China, July 14–18, 2014*, edited by H. Zhang, X. Deng, and Z. Fans, 2014, pp. 1491–1507.
- <sup>32</sup>Lam, C. K. S. and Groth, C. P. T., “Numerical Prediction of Three-Dimensional Non-Equilibrium Gaseous Flows Using the Gaussian Moment Closure,” Paper 2011-3401, AIAA, June 2011.
- <sup>33</sup>Venkatakrishnan, V., “On the Accuracy of Limiters and Convergence to Steady State Solutions,” Paper 93-0880, AIAA, January 1993.
- <sup>34</sup>Harten, A., Lax, P. D., and van Leer, B., “On Upstream Differencing and Godunov-Type Schemes for Hyperbolic Conservation Laws,” *SIAM Rev.*, Vol. 25, No. 1, 1983, pp. 35–61.
- <sup>35</sup>Lomax, H., Pulliam, T. H., and Zingg, D. W., *Fundamentals of Computational Fluid Dynamics*, University of Toronto Press, Toronto, 1981.
- <sup>36</sup>Hicken, J. E. and Zingg, D. W., “A Parallel Newton-Krylov Solver for the Euler Equations Discretized Using Simultaneous Approximation Terms,” *AIAA J.*, Vol. 46, 2008, pp. 2773–2786.
- <sup>37</sup>Northrup, S., *A Parallel Implicit Adaptive Mesh Refinement Algorithm for Predicting Unsteady Fully-Compressible Reactive Flows*, Ph.D. thesis, University of Toronto, 2014.
- <sup>38</sup>Saad, Y., *Iterative Methods for Sparse Linear Systems*, PWS Publishing Company, Boston, 1996.
- <sup>39</sup>Chan, T. and Mathew, T., “Domain Decomposition Algorithms,” *Acta Numerica*, 1994, pp. 61–143.
- <sup>40</sup>Pueyo, A. and Zingg, D. W., “An Efficient Newton-GMRES Solver for Aerodynamic Computations,” Paper 97-1955, AIAA, June 1997.
- <sup>41</sup>Nielsen, E. J., Anderson, W. K., Walters, R. W., and Keyes, D. E., “Application of Newton-Krylov Methodology to a Three-Dimensional Unstructured Euler Code,” Paper 95-1733-CP, AIAA, June 1995.
- <sup>42</sup>Dembo, R. S., Eisenstat, S. C., and Steihaug, T., “Inexact Newton Methods,” *SIAM J. Numer. Anal.*, Vol. 19, No. 2, 1982, pp. 400–408.
- <sup>43</sup>Gropp, W. D., Kaushik, D. K., Keyes, D. E., and Smith, B. F., “High-Performance Parallel Implicit CFD,” *Parallel Computing*, Vol. 27, 2001, pp. 337–362.
- <sup>44</sup>Knoll, D. A. and Keyes, D. E., “Jacobian-Free Newton-Krylov Methods: A Survey of Approaches and Applications,” *J. Comput. Phys.*, Vol. 193, 2004, pp. 357–397.
- <sup>45</sup>Groth, C. P. T. and Northrup, S. A., “Parallel Implicit Adaptive Mesh Refinement Scheme for Body-Fitted Multi-Block Mesh,” Paper 2005-5333, AIAA, June 2005.
- <sup>46</sup>Zhang, Z. J. and Groth, C. P. T., “Parallel High-Order Anisotropic Block-Based Adaptive Mesh Refinement Finite-Volume Scheme,” Paper 2011-3695, AIAA, June 2011.
- <sup>47</sup>Northrup, S. A. and Groth, C. P. T., “Solution of Laminar Combusting Flows Using a Parallel Implicit Adaptive Mesh Refinement Algorithm,” Fourth International Conference on Computational Fluid Dynamics, Ghent, Belgium, July 10–14, 2006, July 2006.
- <sup>48</sup>Groth, C. P. T., Gombosi, T. I., Roe, P. L., and Brown, S. L., “Gaussian-Based Moment-Method Closures for the Solution of the Boltzmann Equation,” *Proceedings of the Fifth International Conference on Hyperbolic Problems — Theory, Numerics, Applications, University of New York at Stony Brook, Stony Brook, New York, U.S.A., June 13–17, 1994*, edited by J. Glimm, M. J. Graham, J. W. Grove, and B. J. Plohr, World Scientific, New Jersey, 1996, pp. 339–346.
- <sup>49</sup>Groth, C. P. T., Roe, P. L., Gombosi, T. I., and Brown, S. L., “On the Nonstationary Wave Structure of a 35-Moment Closure for Rarefied Gas Dynamics,” Paper 95-2312, AIAA, June 1995.
- <sup>50</sup>Groth, C. P. T., Gombosi, T. I., Roe, P. L., and Brown, S. L., “A Gaussian-Based Closure for Rarefied Gases: Derivation, Moment Equations, and Wave Structure,” submitted to the *Journal of Fluid Mechanics*, September 1998.
- <sup>51</sup>Hittinger, J. A., *Foundations for the Generalization of the Godunov Method to Hyperbolic Systems with Stiff Relaxation Source Terms*, Ph.D. thesis, University of Michigan, 2000.
- <sup>52</sup>Vincenti, W. G. and Kruger, C. H., *Introduction to Physical Gas Dynamics*, R. E. Krieger Publishing, Huntington, NY, 1975.
- <sup>53</sup>Kennard, E. H., *Kinetic Theory of Gases*, McGraw-Hill, New York, 1938.
- <sup>54</sup>Knudsen, M., “Die molekulare Wärmeleitung der Gase und der Akkommodationskoeffizient,” *Annalen der Physik*, Vol. 339, No. 4, 1911, pp. 593–656.
- <sup>55</sup>Struchtrup, H., “Heat Transfer in the Transition Regime: Solution of Boundary Value Problems for Grad’s Moment Equations via Kinetic Schemes,” *PhysRevE*, Vol. 65, 2002, pp. 041204–1–041204–16.
- <sup>56</sup>Struchtrup, H., “Kinetic Schemes and Boundary Conditions for Moment Equations,” *Zeitschrift für angewandte Mathematik und Physik*, Vol. 51, 2000, pp. 346–365.

<sup>57</sup>Torrilhon, M., "Slow Gas Microflow Past a Sphere: Analytic Solution Based on Moment Equations," *Phys. Fluids*, Vol. 22, No. 072001, 2010, pp. 1–16.

<sup>58</sup>Coudeville, H., Trepaud, P., and Brun, E. A., "Drag Measurements in Slip and Transition Flow," *Rarefied Gas Dynamics*, edited by J. H. de Leeuw, Vol. I, Academic Press, New York, 1965, pp. 444–466.

<sup>59</sup>John, B., Gu, X. J., and Emerson, D. R., "Investigation of Heat and Mass Transfer in a Lid-Driven Cavity Under Nonequilibrium Flow Conditions," *Numer. Heat Trans. B*, Vol. 52, 2010, pp. 287–303.

<sup>60</sup>John, B., Gu, X. J., and Emerson, D. R., "Effects of Incomplete Surface Accomodation on Non-equilibrium Heat Transfer in Cavity Flow; A Parallel DSMC Study," *Computer & Fluids*, Vol. 45, 2011, pp. 197–201.